Deformation of Filament Bundles

Hannah Tatman

Supervised by: Dr Chris Prior

Department of Mathematical Sciences
Durham University

'This piece of work is a result of my own work except where it forms an assessment based on group project work. In the case of a group project, the work has been prepared in collaboration with other members of the group. Material from the work of others not involved in the project has been acknowledged and quotations and paraphrases suitably indicated.'

I would like to acknowledge and thank a number of people who have been crucial to the success of this project. Mainly I would like to thank Chris Prior who has been a wonderful supervisor who has always been happy to run hundreds of iterations of faulty code and generously explain the ins and outs of Fortran. I would also like to thank Jack Panter and Halim Kusumaatmaja for their work on this topic previously which has provided such a solid foundation to work off. Finally, I'd like to give a special thank you to my family and friends - Jed, Tom, Faith and Rachel, your enthusiasm in this project has been much appreciated - along with anyone else who has had to listen to me non-stop repeat the phrase 'bendy but not stretchy'.

Contents

Chapter 1

Introduction

Central to the study of biological materials is the notion of a filament bundle. Filament bundles are, as the name implies, bundles of fibres embedded in an elastic matrix and appear frequently in biological systems, ranging from bundles of actin proteins held together by crosslinks [1], muscle fibres [2] or peripheral nerve fascicles [3].

1.1 Motivation

Deformation of these structures in the form of compression, bending, stretching, twisting or any combination of such behaviours can have potentially very serious medical and physiological implications. Axons are the site of electrochemical transmission in biological systems and prolonged exposure to compression such as that seen in carpal tunnel syndrome can cause degradation of myelin or a blockage of axonal transport. This in turn can cause numbness and pain and can eventually lead to muscle degradation and impaired mobility [4]. Considering more acute behaviour, the most common cause of traumatic spinal cord injury is compression by bone fragments following a fracture or dislocation injury [5]. It is therefore necessary to have accurate models of these structures under loading to better predict and prevent such mechanical damage.

1.2 Previous Models

There has been much previous research into the structural and mechanical properties of fibre bundles but modelling their behaviour presents particular complexity, the sheer number of interacting parts means that they exhibit highly non-linear interactive feedback which is difficult to analyse and computationally expensive to model. As such, previous research has typically modelled individual filaments [6] and where bundle mechanics have been studied these models have generally either taken the form of continuum models which account for some non linear behaviour but do not explicitly model individual filaments [7] or bundle models which make a range of assumptions to reduce the unpredictability of the non linear behaviour and allow for quantitiative analysis [8].

This project however, is an extension of a model devised by Chris Prior et al. [9]. This utilised discrete differential geometry to generate a topologically exact model of a planar cross section of a bundle to find and categorise deformation configurations. This research was able to replicate a wide variety of behaviours and so a lot of the method has been utilised again here. However, due to the limitations of considering only a 2D model, this work was

unable to consider the effect of rotation or to find configurations which exhibit torsion. Following a head trauma, acute torsion of axons is strongly linked to diffuse axonal injury [10] - which a severe traumatic brain injury characterised by scattered lesions throughout the grey matter in the brain and is one of the leading cause of persistent vegetative state [11].

As such, it was important that a model was able to capture among other things, this kind of twisting behaviour.

1.3 Nerve Structure

To be able to effectively model a nerve fascicle, it is helpful to have a broad understanding of the anatomical structure of a nerve. The most fundamental structure of the nervous system is the axon – this is the site of electrical impulse transmission and is what we would typically think of as a "nerve". An axon is surrounded by a layer of myelin, a lipid which provides insulation against diffusion, these so called myelinated axons (neurons) are surrounded by connective tissue called the endoneurium and together the bundle of myelinated axons embedded in the endoneurium are surrounded by another rigid layer of connective tissue known as the perineurium. The structure enclosed within the perineurium is a nerve fascicle and is the primary object of study of this research. For further context, multiple fascicles are grouped together along with blood vessels and these bundles are further surrounded by another layer of connective tissue known as the epineurium. The epineurium constitutes the boundary of the nerve. Due to the complexity of the nerve and the geometric irregularity of their structures, it is appropriate for this model to simplify the considerations significantly. As such we will reduce the "bundle of bundles" system and consider just the nerve fascicle. Figure 1.1 is a helpful diagram depicting this microstructure [12].

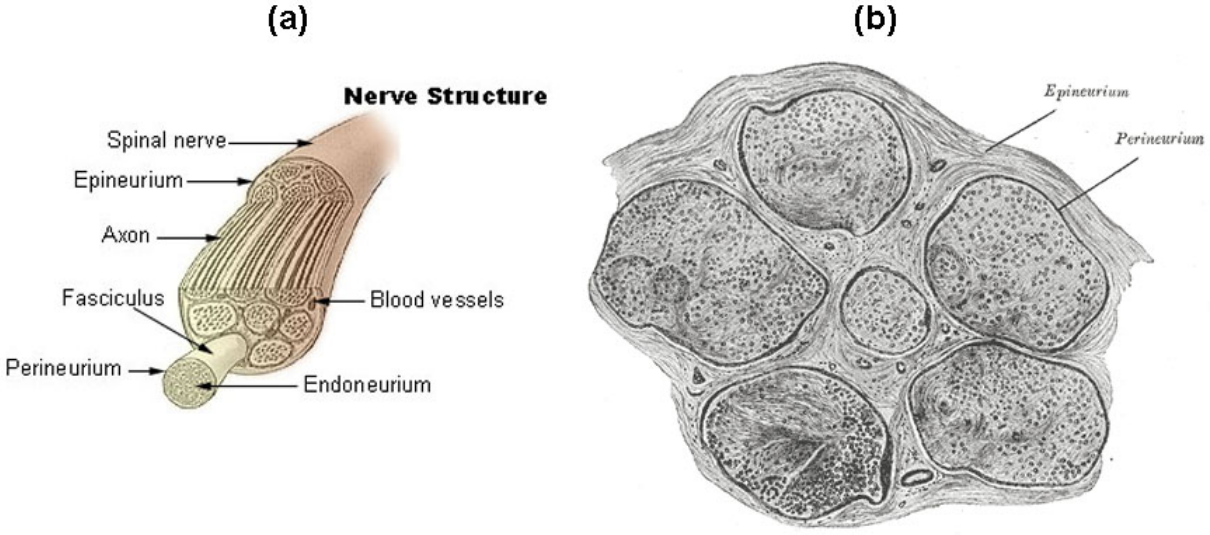

Figure 1.1: The structure of a Neuron

Chapter 2

Continuous Curve Theory

To effectively derive a model of a bundle of elastic rods, it is first appropriate to establish the mathematical context of rod theory which itself requires a thorough understanding of the theory of curves more broadly. We will therefore, first cover the background of continuous space curves before considering processes of discretisation focusing particularly on the derivation of a notion of discrete curvature. We will finally consider how the 1-dimensional curve is extended to 3 dimensions by considering rods parameterised by a material curve with a cross sectional area, so called rod theory. This is a vast area of non-linear solid mechanics and much is beyond the scope of this project so will only be touched on briefly.

A smooth, parameterised space curve, henceforth referred to as a curve is an smooth (infinitely, continuously differentiable) map $\mathbf{r} : I \to \mathbb{R}^3$ where $I = [p_A, p_B] \subset \mathbb{R}$ and the parameter p maps to the point $\mathbf{r}(p)$.
The curve is described as regular if

$$\frac{d\mathbf{r}}{dp} \neq 0 \quad \text{for all } p \in I. \tag{2.1}$$

For such regular curves, we can define the non-vanishing tangent vector

$$\mathbf{t}(p) = \frac{d\mathbf{r}}{dp}. \tag{2.2}$$

This allows us to define the arc-length between any points (p_0, p) on $\mathbf{r}(p)$ as such,

$$s(p) = \int_{p_0}^{p} \|\mathbf{t}(u)\| du, \tag{2.3}$$

and $s(p)$ has the property

$$\frac{ds}{dp} = \|\mathbf{t}(p)\|. \tag{2.4}$$

This is helpful since we can now parameterise $\mathbf{r}$(p) in terms of arc-length by setting

$$p = s(p), \tag{2.5}$$

and therefore

$$\|\mathbf{t}(p)\| = \frac{ds}{dp} = 1, \tag{2.6}$$

which leads to the analogous description of arc-length parameterised curves as unit-speed curves.

For any finite regular curve of length L we can now define a map $\mathbf{r} : [0, L] \to \mathbb{R}^3$ and this map will parameterise the curve. If someone were to walk along this curve from $\mathbf{r}(s(p))$ to $\mathbf{r}(s(p+\epsilon))$, they would travel a distance of ϵ.

It is possible to uniquely determine an arc-length parameterised space curve by two scalar invariants - the curvature κ and torsion τ [13]. To do so is it necessary to first consider the specific case of plane curves.

2.1 The Planar Case

For any unit-speed plane curve $\boldsymbol{\gamma}(s)$ in $\mathbb{R}^2$ we can define its tangent $\mathbf{t}(s)$ as in 2.2 and define the unit normal $\mathbf{n}(s)$ as the rotation of $\mathbf{t}$ by $\pi/2$ anticlockwise noting that $\|\mathbf{t}(s)\| = 1$, so $\mathbf{t}$ and $\mathbf{n}$ are orthonormal.

We can differentiate the unit speed relation $\mathbf{t} \cdot \mathbf{t} = 1$ to obtain

$$2\frac{d\mathbf{t}}{ds} \cdot \mathbf{t} = 0, \tag{2.7}$$

which implies $\frac{d\mathbf{t}}{ds}$ and $\mathbf{t}$ are orthogonal. We can thus define a scalar function $\kappa(s)$ such that,

$$\frac{d\mathbf{t}}{ds} = \kappa\mathbf{n}. \tag{2.8}$$

Following the same process we also obtain that $\frac{d\mathbf{n}}{ds}$ and $\mathbf{n}$ are orthogonal and so

$$\frac{d\mathbf{n}}{ds} = \alpha\mathbf{t}, \tag{2.9}$$

but noting that $\mathbf{t} \cdot \mathbf{n} = 1$ we obtain

$$\begin{aligned} \mathbf{n} \cdot \frac{d\mathbf{t}}{ds} + \mathbf{t} \cdot \frac{d\mathbf{n}}{ds} &= 0, \\ \mathbf{n} \cdot \kappa\mathbf{n} + \mathbf{t} \cdot \alpha\mathbf{t} &= 0, \\ \kappa + \alpha &= 0, \\ \alpha &= -\kappa, \\ \frac{d\mathbf{t}}{ds} = \kappa\mathbf{n}, \quad \frac{d\mathbf{n}}{ds} &= -\kappa\mathbf{t}. \end{aligned} \tag{2.10}$$

The quantity $\kappa(s)$ is the curvature and is a measure of the rotation of $\mathbf{t}$ as we move along the curve at unit speed. This makes intutive sense - curves which bend more have

tangents which change direction more rapidly. κ is positive when the curve bends in the direction of the unit normal (anti-clockwise) and is negative for clockwise bending.

A different way of thinking about curvature

An alternative but equivalent definition which will be of particular use when discretising is that $\kappa(s)$ can be defined as the inverse of the radius of an osculating circle [14]. An osculating circle at point s on curve $\boldsymbol{\gamma}$ is the circle which has the same tangent as the curve at point s.

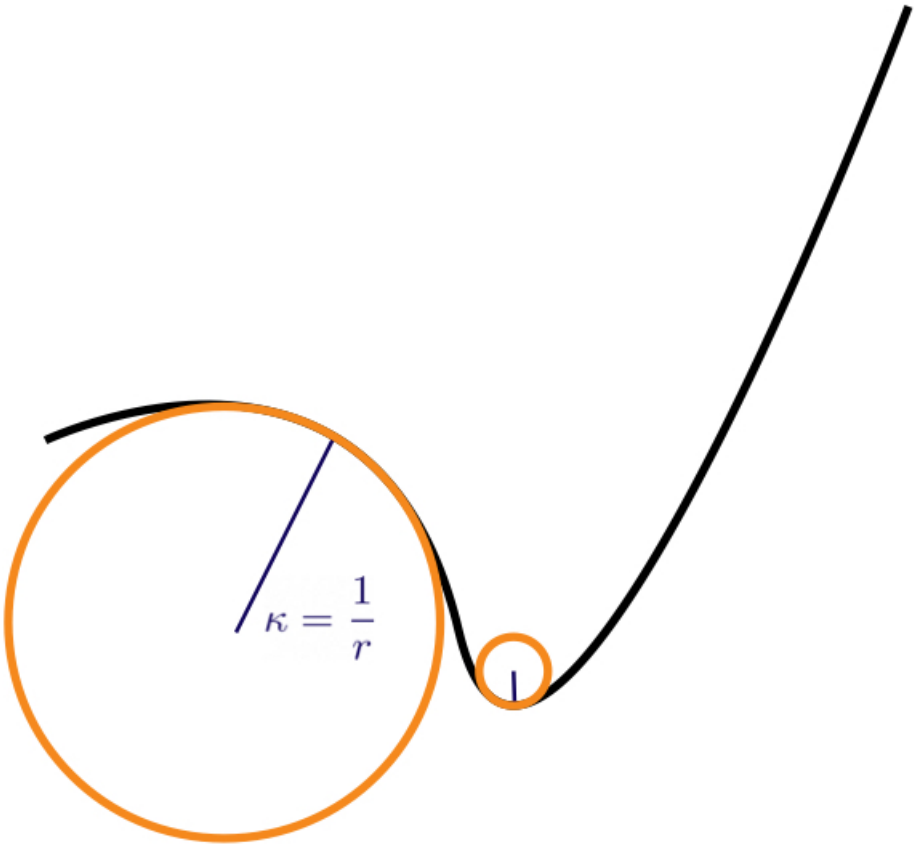

Figure 2.1: κ defined using the osculating circle method

2.2 Space Curves

The notion of how much a curve bends can be readily extended to space curves in $\mathbb{R}^3$ but the concept of bending in a positive or negative direction relative to the normal loses its significance since there is no straightforward way to specify a normal to a curve in $\mathbb{R}^3$ [15]. We consider again a unit speed curve $\boldsymbol{\gamma}(s)$ this time in $\mathbb{R}^3$ with tangent

$$\mathbf{t} = \boldsymbol{\gamma}'(s), \tag{2.11}$$

To circumvent the issue of signed curvature we instead define the new (unsigned) curvature $\mathbb{R}^3$ as in Eq(2.8)

$$\frac{d\mathbf{t}}{ds} = \kappa\mathbf{n}. \tag{2.12}$$

Since there is no longer a requirement that κ be signed in $\mathbb{R}^3$, we instead define

$$\kappa = \left\| \frac{d\mathbf{t}}{ds} \right\|. \tag{2.13}$$

While a regular planar curve could be uniquely described by one scalar invariant, the curvature κ, for a space curve it is necessary to define another scalar invariant - the torsion τ. To do so, it is necessary to establish the notion of an orthonormal frame.

Framing a curve

In the planar case $\{\mathbf{t}, \mathbf{n}\}$ form an adapted orthonormal frame to a unit speed curve. It is helpful to think of an adapted frame as a frame of reference as an observer travels along the curve[13]. The frame moves along the curve and will rotate but the vectors $\mathbf{t}$ and $\mathbf{n}$ remain orthogonal.

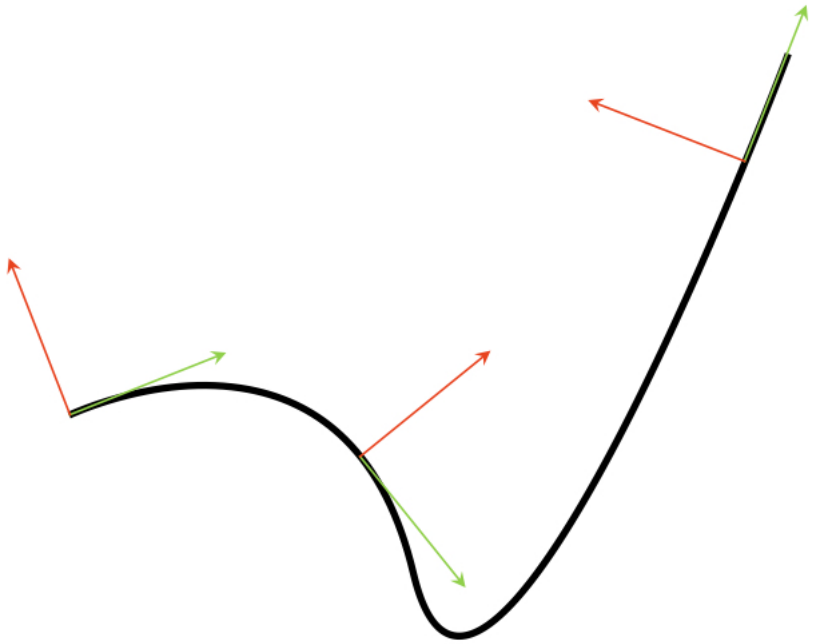

Figure 2.2: A planar curve with an orthonormal frame $\{\mathbf{t}, \mathbf{n}\}$. Tangent vectors $\mathbf{t}$ are green while normal vectors $\mathbf{n}$ are red.

Since a planar curve in $\mathbb{R}^2$ has a 2 dimensional orthonormal frame it is intuitive that a space curve in $\mathbb{R}^3$ would have a 3 dimensional orthonormal frame. The third vector - known as the binormal - can be defined simply as

$$\mathbf{b} = \mathbf{t} \times \mathbf{n}. \tag{2.14}$$

Which has the property

$$\|\mathbf{b}\| = \|\mathbf{t}\|\|\mathbf{n}\| \sin\theta = 1 \cdot 1 \cdot 1 = 1, \tag{2.15}$$

since $\theta = \pi/2$. We now have that $\{\mathbf{t}, \mathbf{n}, \mathbf{b}\}$ form an adapted orthonormal moving frame along the curve. This frame is known as the Frenet Frame and will be of great significance moving forward. Note, there is no natural way to define $\mathbf{n}$ or $\mathbf{b}$ when the curvature is 0 [13].

Since $\mathbf{b}$ has unit length, we can follow the same process as in (2.7 - 2.8) to show that

$$\frac{d\mathbf{b}}{ds} \cdot \mathbf{b} = 0, \tag{2.16}$$

And utilise 2.12 to obtain

$$\frac{d\mathbf{b}}{ds} = \mathbf{t} \times \frac{d\mathbf{n}}{ds} + \frac{d\mathbf{t}}{ds} \times \mathbf{n}, \tag{2.17}$$

$$= \mathbf{t} \times \frac{d\mathbf{n}}{ds} + \kappa\mathbf{n} \times \mathbf{n}, \tag{2.18}$$

$$= \mathbf{t} \times \frac{d\mathbf{n}}{ds}. \tag{2.19}$$

Furthermore

$$\frac{d\mathbf{b}}{ds} \cdot \mathbf{b} = 0, \tag{2.20}$$

$$\frac{d\mathbf{b}}{ds} \cdot \mathbf{t} = 0. \tag{2.21}$$

This implies that

$$\frac{d\mathbf{b}}{ds} = -\tau\mathbf{n}, \tag{2.22}$$

for some scalar quantity τ since $\{\mathbf{t}, \mathbf{n}, \mathbf{b}\}$ form an orthonormal frame and $\frac{d\mathbf{b}}{ds}$ is orthogonal to $\mathbf{t}$ and $\mathbf{b}$. The quantity τ is the torsion of the curve and geometrically describes the rate at which the curve twists out of its osculating plane (the plane containing $\mathbf{t}$ and $\mathbf{n}$). A more compact helix will have a lower torsion while a less tight more stretched out helix will generally have a higher torsion. If curvature measures the deviation of a curve from being straight, torsion measures the deviation of a curve from being planar.

We also have

$$\mathbf{n} = \mathbf{b} \times \mathbf{t}, \tag{2.23}$$

$$\frac{d\mathbf{n}}{ds} = \mathbf{b} \times \frac{d\mathbf{t}}{ds} + \frac{d\mathbf{b}}{ds} \times \mathbf{t}, \tag{2.24}$$

$$= \mathbf{b} \times \kappa\mathbf{n} + -\tau\mathbf{n} \times \mathbf{t}, \tag{2.25}$$

$$= -\kappa\mathbf{t} + \tau\mathbf{t}. \tag{2.26}$$

These moving equations which govern the change of the adapted frame along the curve are known as the Frenet-Serret equations and can be conveniently written in matrix form.

$$\begin{pmatrix} \frac{d\mathbf{t}}{ds} \\ \frac{d\mathbf{n}}{ds} \\ \frac{d\mathbf{b}}{ds} \end{pmatrix} = \begin{pmatrix} 0 & \kappa & 0 \\ -\kappa & 0 & \tau \\ 0 & -\tau & 0 \end{pmatrix} \begin{pmatrix} \mathbf{t} \\ \mathbf{n} \\ \mathbf{b} \end{pmatrix} \tag{2.27}$$

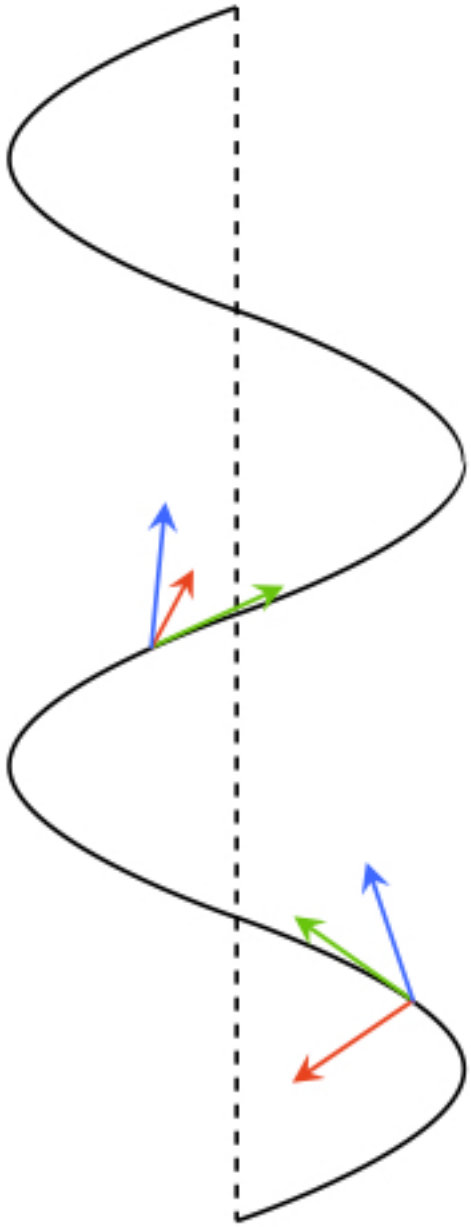

Figure 2.3: A helix with an adapted frame $\{\mathbf{t}, \mathbf{n}, \mathbf{b}\}$. Tangent vectors $\mathbf{t}$ are green, normal vectors $\mathbf{n}$ are red and binormal vectors $\mathbf{b}$ are blue

Chapter 3

Rod Theory

Having established the mathematical preliminaries in determining and analysing the geometry of a curve, it is now appropriate to consider how this is extended to model solid bodies.

The most fundamental component of this system is that of the discrete rod so it is necessary to touch briefly on the aspects of the theory which are most relevant to this model. Rod theory and specifically discrete rod theory are vast areas in non-linear solid mechanics and unfortunately much is beyond the scope of this project. For a more detailed explanation of the theory of the continuous model, the reader is directed to chapter 4 of [16] which provides a very thorough background. A reader more interested in the discrete rod theory is encouraged to read [17], specifically chapters 5 & 6, which enter into further detail about discrete curve framing. Together, these two texts have informed much of this section.

3.1 Kirchhoff Rod Theory

Kirchhoff elastic rod theory, which much of this work draws from is a formulation of rod theory (slender body elastica) which is capable of modelling both bending and torsion and does so by assigning a bending and a twisting energy to an elastic rod [18, 17, 16]. Both are measures of the deformation of the material curve $\mathscr{L}$ of the rod relative to its reference state $\mathscr{L}_0$. The material curve is usually the center-line of the rod and defines the propagation of an orthonormal adapted frame along the rod [17].

There are varied conventions on how to define the adapted frame of a rod $\{\mathbf{d}_1, \mathbf{d}_2, \mathbf{d}_3\}$ but generally $\mathbf{d}_3$ is defined as the tangent vector while $\mathbf{d}_1$ and $\mathbf{d}_2$ represent quantities related to the cross section of the body [16].

The bending of a rod is intuitively how much the rod bends away from it's reference configuration. In our model the reference is straight but much work has been done on biological rod structures which have non vanishing intrinsic curvature. Particular examples include DNA and curly hair which both have naturally helical structures [19, 20].

The twisting of a rod is how much the non-tangential vectors $\{\mathbf{d}_1, \mathbf{d}_2\}$ rotate around the tangent along the rod. If someone were to fix one end of an elastic rod and rotate the other by $\pi/2$ then the total twist of the rod would be lower than if someone were to twist the rod through an angle of 2π. Crucially, the torsional stiffness - how large the torsional

moment applied must be for the rod to twist - is calculated as:

$$\mu \frac{\pi R^4}{4}, \tag{3.1}$$

where R is the cross sectional radius of the rod and μ is a parameter of the material [21]. Since we have chosen to model fibres with very small cross sections the torsional stiffness would be almost 0 and the subsequent impact of twisting energy on energy mimina would be negligible. Coupled with this, it was deemed that there is no loading which is likely to cause individual filament twisting since all loads were applied to the exterior of the bundle. A modelling decision was therefore made to ignore the impact of individual filament twist.

Chapter 4

Discrete Curves

4.1 The Discrete Case

A discrete curve Γ consists of a set of (n+1) vertices $\{\mathbf{x}_0, \mathbf{x}_1, ...\mathbf{x}_n\}$ and n edges between adjacent vertices $\{\mathbf{v}_1, \mathbf{v}_2, ...\mathbf{v}_n\}$ [18]. The decision to number the nodes from 0 while the first edge is numbered 1 is not something which is consistently held to in the literature (some have both edges and nodes being numbered from 0 or 1) but is one which is helpful for this specific model as will become clear.

To model a discrete rod, the same principle is applied as in Section 3.1 where a discrete material curve is defined and an orthonormal basis is assigned to each edge $\mathbf{v}_i$ of the rod.

4.1.1 Discrete Curvature

As touched on above, a fundamental energy consideration is that of bending which requires a notion of curvature. The continuous notion of curvature as described in Eq(2.13) is obviously not applicable to the discrete setting since we would have 0 curvature along edges and infinite curvature at vertices. Instead we consider the discrete analogue of the equivalent definition of curvature seen in Figure(2.1).

We fix $|\mathbf{v}_i| = |\mathbf{v}_{i+1}| = \mathrm{r}$.
This fixes the edge length of the curve. For a reference curve Γ_0 which is a straight line, as in the case of this model, we consider the length L of the reference curve and define

$$r = \frac{L}{n}. \tag{4.1}$$

By the scalar product between $\mathbf{v}_i$ and $\mathbf{v}_{i+1}$ we take the angle between $\mathbf{v}_i$ and $\mathbf{v}_{i+1}$ to be α_i and denote

$$\begin{aligned} p_i &= \frac{\mathbf{v}_i \cdot \mathbf{v}_{i+1}}{|\mathbf{v}_i||\mathbf{v}_{i+1}|}, \\ &= -\cos(\alpha_i). \end{aligned}$$

Where we have taken that $\mathbf{v}_i$ points towards node $\mathbf{x}_i$ and $\mathbf{v}_{i+1}$ points away from node $\mathbf{x}_i$. The full derivation of this discrete curvature is included in Appendix B but we find

$$\frac{1}{R_i} = \kappa_i = 2\sqrt{\frac{1-p_i}{1+p_i}}. \tag{4.2}$$

.
We are now in a position to consider how we model a filament bundle.

4.2 The Spherical co-ordinate system

The Cartesian coordinate of each node is parametrised in spherical polar coordinates (r, θ, ϕ).These are the standard radial, azimuthal and polar coordinates with the distinction that here ϕ represents incline angle from the x-y plane rather than the polar angle from the z-axis. Whereas the standard polar angle varies between $[0, \pi]$, ϕ instead varies between $[-\frac{\pi}{2}, \frac{\pi}{2}]$ The Cartesian vector (x, y, z) parameterised by (r, θ, ϕ) is

$$(x, y, z) = r(\cos\theta\cos\phi, \sin\theta\cos\phi, \sin\phi). \tag{4.3}$$

4.3 The set up of the system

We consider a bundle of $l * m$ inextensible filaments, each a discrete curve composed of n edges and $n + 1$ vertices. The filaments each have the same length L, and undeformed, the bundle has width W and height H. Further quantities which are considered include,

- $r = \frac{L}{n}$, the distance between each node in the same chain
- $d_y = \frac{W}{m-1}$, the undeformed horizontal distance between the j^{th} and $(j+1)^{th}$ filament
- $d_z = \frac{H}{l-1}$, the undeformed vertical distance between the i^{th} and $(i+1)^{th}$ filament

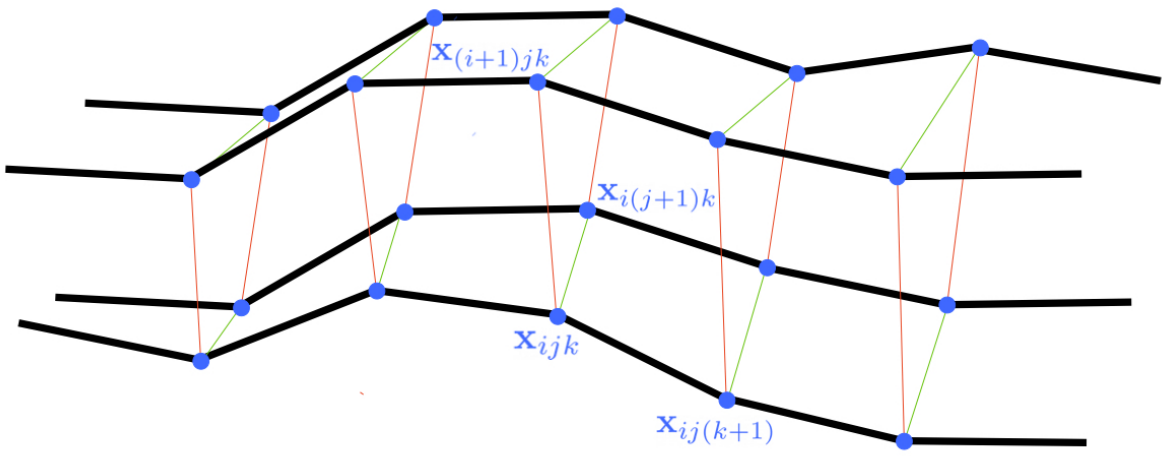

Figure 4.1: The structure of adjacent filaments in a deformed configuration. Here black lines represent edges, green lines denote nodes of differing j component and red lines denote nodes of differing z component

4.4 Node positioning

The first node on each filament $\mathbf{x}_{ij0}$ has fixed position and the positions of subsequent nodes are

$$\mathbf{x}_{ijk} = \mathbf{x}_{ij0} + r \sum_{s=1}^{k} (\cos\theta_{ijs} \cos\phi_{ijs}, \sin\theta_{ijs} \cos\phi_{ijs}, \sin\phi_{ijs}) \quad k \in (1, ...n), \tag{4.4}$$

where

$$\mathbf{x}_{ij0} = \left(0, (j-1)\frac{W}{m-1} + (i-1)\frac{H}{l-1}\right). \tag{4.5}$$

Chapter 5

Energy

The aim of the model is to find static deformed configurations of the bundle under applied loads. To do so it is appropriate to derive an energy functional of the whole system, parameterised by the angles which define the positioning of each of the nodes and then numerically search for a minimal energy configuration.

The energy functional can be considered as the sum of

- E_b the bending energy
- E_c the penalty imposed on deviation from boundary conditions
- E_s the interaction energy between filaments
- E_t the penalty on local self - intersection
- E_f the moments of the applied external forces

5.1 Bending Energy

The bending energy along the $(i,j)^{th}$ filament can be computed as

$$E_{b(i,j)} = \sum_{k=1}^{n-1} \frac{r}{2} B_{ijk} \kappa_{ijk}^2, \tag{5.1}$$

where we have utilised the discrete curvature κ, derived in B.12.

$$\kappa = \frac{2}{r}\sqrt{\frac{1-p_{ijk}}{1+p_{ijk}}},$$

where

$$p_i = \frac{\mathbf{v}_i \cdot \mathbf{v}_{i+1}}{|\mathbf{v}_i||\mathbf{v}_{i+1}|}. \tag{5.2}$$

In our coordinate system,

$$\begin{aligned} \mathbf{v}_i &= (\cos\theta_i \cos\phi_i, \sin\theta_i \cos\phi_i, \sin\phi_i), \\ \mathbf{v}_{i+1} &= (\cos\theta_{i+1} \cos\phi_{i+1}, \sin\theta_{i+1} \cos\phi_{i+1}, \sin\phi_{i+1}). \end{aligned} \tag{5.3}$$

We therefore have

$$\begin{aligned} p_i = \frac{1}{r^2}[&\cos\theta_i \cos\phi_i \cos\theta_{i+1} \cos\phi_{i+1} \\ &+ \sin\theta_i \cos\phi_i \sin\theta_{i+1} \cos\phi_{i+1} \\ &+ \sin\phi_i \sin\phi_{i+1}], \end{aligned}$$

and the total bending energy in the whole system can be computed as

$$E_b = \sum_{i=1}^{l} \sum_{j=1}^{m} \sum_{k=1}^{n-1} \frac{2B_{ijk}}{r} \frac{1 - p_{ijk}}{1 + p_{ijk}}. \tag{5.4}$$

For this model, 2 bending coefficients B_{int} and B_{ext} were considered for internal and external filaments respectively. That is

$$B_{ijk} = \begin{cases} B_{int}, & 1 < i < l \quad \text{and} \quad 1 < j < m \\ B_{ext}, & i = 1, l \quad j = 1, m \end{cases} \tag{5.5}$$

The ratio

$$B_{RAT} = \frac{B_{ext}}{B_{int}}, \tag{5.6}$$

represents the rigidity of the outer sheath relative to the internal structure as exhibited by the perineurium.

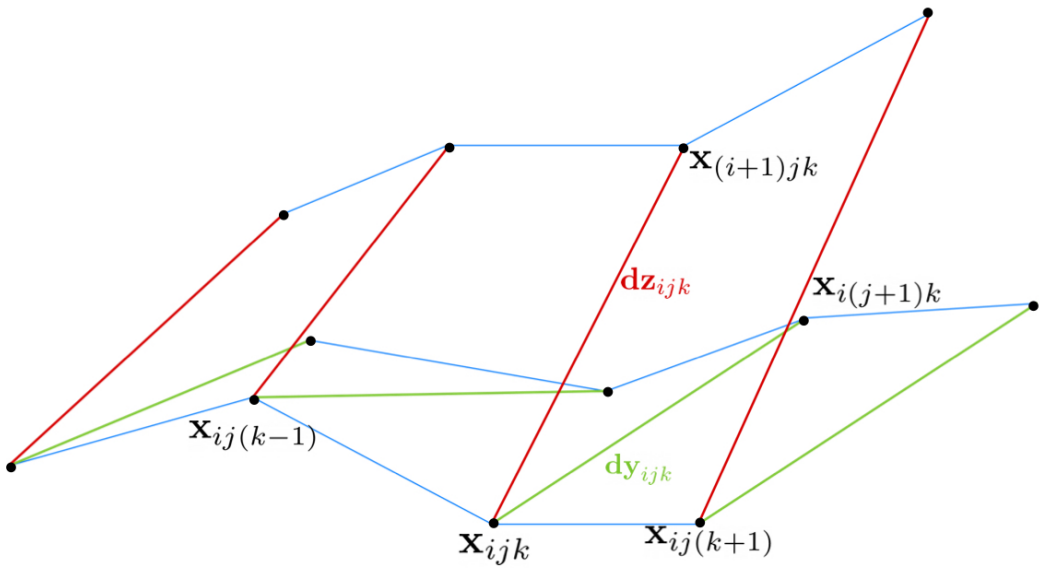

Figure 5.1: Straight spring potentials

5.2 Interaction Energy

The interaction between nodes of adjacent filaments is modelled using a non-dimensionalised Hookean spring potential of the form:

$$f(d) = \frac{1}{2}K\left(\frac{d - d_0}{d_0}\right)^2. \tag{5.7}$$

where d is the deformed spring length and d_0 is the initial spring length.

5.2.1 Straight springs

We first consider the interaction which occurs when filaments are pulled apart or compressed together and define the deformed distances from $\mathbf{x}_{ijk}$ as

$$d_{y(ijk)} = \left|\mathbf{d}_{y(ijk)}\right| = \left|\mathbf{x}_{i(j+1)k} - \mathbf{x}_{ijk}\right|, \tag{5.8}$$

$$d_{z(ijk)} = \left|\mathbf{d}_{z(ijk)}\right| = \left|\mathbf{x}_{(i+1)jk} - \mathbf{x}_{ijk}\right|. \tag{5.9}$$

The strain energy function is taken as uniform within the structure as

$$f_y(d_{y(ijk)}) = \frac{K_{y(ijk)}}{2}\left(\frac{d_{y(ijk)} - d_y}{d_y}\right)^2, \tag{5.10}$$

$$f_z(d_{z(ijk)}) = \frac{K_{z(ijk)}}{2}\left(\frac{d_{z(ijk)} - d_z}{d_z}\right)^2. \tag{5.11}$$

Where $K_{y(ijk)}, K_{z(ijk)}$ are the spring coefficients for $\mathbf{d}_{y(ijk)}$ and $\mathbf{d}_{z(ijk)}$. Similarly to the case of bending, we have chosen to keep the spring coefficient uniform throughout the structure for all spring directions. The interaction energy from straight springs along the $(i,j)^{th}$ filament can be computed as

$$E_{s(i,j)} = \sum_{k=0}^{n}\Big[f_y(d_{y(ijk)}) + f_z(d_{z(ijk)})\Big]. \tag{5.12}$$

The total interaction energy in the system from straight springs is therefore

$$E_s = \sum_{i=1}^{l}\sum_{j=1}^{m-1}\sum_{k=0}^{n} f_y(d_{y(ijk)}) + \sum_{i=1}^{l-1}\sum_{j=1}^{m}\sum_{k=0}^{n} f_z(d_{z(ijk)}). \tag{5.13}$$

5.2.2 Diagonal Springs

The previous treatment of interaction is sufficient to model the impact of an elastic matrix when adjacent filaments separate or compress but when the bundle is bent, the distance between nodes of the same k component may only change negligibly as the cross sections of the bundle remain normal to the central material curve. It is clear, therefore that there is a need to consider stretching between nodes of different k component to effectively capture the stretching here. To model this, we also consider spring distances for adjacent filaments

of different k component.
We define the deformed diagonal distances from $\mathbf{x}_{ijk}$ as

$$d^{+}_{y(ijk)} = \left|\mathbf{d}^{+}_{y(ijk)}\right| = \left|\mathbf{x}_{i(j+1)(k+1)} - \mathbf{x}_{ijk}\right|, \tag{5.14}$$

$$d^{-}_{y(ijk)} = \left|\mathbf{d}^{-}_{y(ijk)}\right| = \left|\mathbf{x}_{i(j+1)(k-1)} - \mathbf{x}_{ijk}\right|, \tag{5.15}$$

$$d^{+}_{z(ijk)} = \left|\mathbf{d}^{+}_{z(ijk)}\right| = \left|\mathbf{x}_{(i+1)j(k+1)} - \mathbf{x}_{ijk}\right|, \tag{5.16}$$

$$d^{-}_{z(ijk)} = \left|\mathbf{d}^{-}_{z(ijk)}\right| = \left|\mathbf{x}_{(i+1)j(k-1)} - \mathbf{x}_{ijk}\right|. \tag{5.17}$$

$$\tag{5.18}$$

We also consider the un-deformed distances

$$d^{\pm}_{y} = \sqrt{r^2 + d^2_{y}}, \tag{5.19}$$

$$d^{\pm}_{z} = \sqrt{r^2 + d^2_{z}}. \tag{5.20}$$

The strain energy function for diagonal springs is (as above):

$$f_y(d^{\pm}_{y(ijk)}) = \frac{K^{\pm}_{y(ijk)}}{2}\left(\frac{d^{\pm}_{y(ijk)} - d^{\pm}_{y}}{d^{\pm}_{y}}\right)^2, \tag{5.21}$$

$$f_z(d^{\pm}_{z(ijk)}) = \frac{K^{\pm}_{z(ijk)}}{2}\left(\frac{d^{\pm}_{z(ijk)} - d^{\pm}_{z}}{d^{\pm}_{z}}\right)^2. \tag{5.22}$$

The interaction energy from diagonal springs along the $(i,j)^{th}$ filament can be computed as

$$E^{+}_{s(i,j)} = \sum_{k=0}^{n-1}\left[f_y(d^{+}_{y(ijk)}) + f_z(d^{+}_{y(ijk)})\right], \tag{5.23}$$

$$E^{-}_{s(i,j)} = \sum_{k=1}^{n}\left[f_y(d^{-}_{y(ijk)}) + f_z(d^{-}_{y(ijk)})\right]. \tag{5.24}$$

The total interaction energy in the system from diagonal springs is therefore

$$E^{+}_{s} = \sum_{i=1}^{l}\sum_{j=1}^{m-1}\sum_{k=0}^{n-1} f_y(d^{+}_{y(ijk)}) + \sum_{i=1}^{l-1}\sum_{j=1}^{m}\sum_{k=0}^{n-1} f_z(d^{+}_{z(ijk)}), \tag{5.25}$$

$$E^{-}_{s} = \sum_{i=1}^{l}\sum_{j=1}^{m-1}\sum_{k=1}^{n} f_y(d^{-}_{y(ijk)}) + \sum_{i=1}^{l-1}\sum_{j=1}^{m}\sum_{k=1}^{n} f_z(d^{-}_{z(ijk)}). \tag{5.26}$$

and the total interaction energy in the whole system is

$$E_{snt} = E_s + E^{+}_{s} + E^{-}_{s}. \tag{5.27}$$

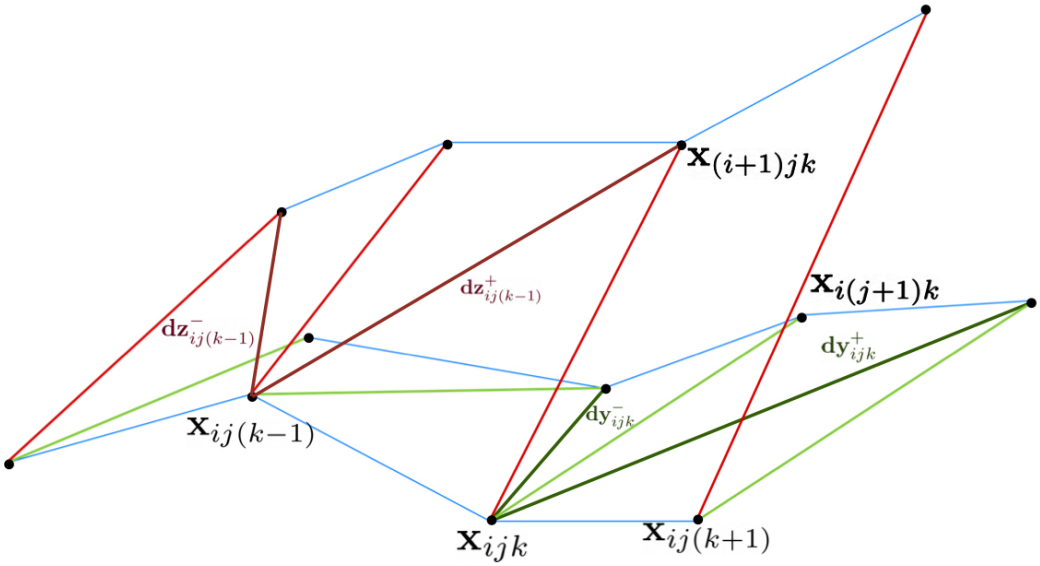

Figure 5.2: Diagonal spring potentials

5.3 Self Intersection Penalty

This model includes a very high number of individual filaments and so preventing self intersection represents a particular challenge from both a modelling and computation time perspective. In the related field of hair simulation it has been noted that between 80-90% of animation time is taken up with collision detection and response [22][23]. Many of the approaches which have previously been taken require advanced understanding of computer and simulation which is beyond the scope of this project. We also found that with the range of parameters and existing energy considerations non-local self intersection was rare and so the problem could be reduced to penalising only local self intersection. It is therefore necessary to devise a different approach which will perform the same objective with a lower prerequisite understanding of computational geometry.

The goal of the approach is to impose a penalty which is sufficiently large for occasions of self intersection that it renders any configurations which exhibit this virtually impossible as energy minima. Conversely, the penalty needs to be negligible for configurations which do not exhibit self-intersection since the biological analogue of this penalty is the boundary surface of an individual axon: compression of surrounding connective tissue is modelled by E_{snt} as described in section 5.2.

The method we attempted drew on the method of [9] in 2 dimensions which penalised internal area compression. The natural extension to 3 dimensions is to penalise internal volume compression by imposing an energy penalty on internal volumes in the deformation

configuration becoming very small relative to their undeformed volume. The challenge is then to find a way of systematically splitting the highly irregular structure into volumes for which it is easy to calculate such volumes. The following method was taken.

The structure is divided into local internal volumes bound by 12 edges formed by 4 rods, 4 **dy** vectors and 4 **dz** vectors (as shown in Fig 5.3). This volume can then be further subdivided into 5 tetrahedrons. The internal tetrahedron can be ignored since the 8 vertex nodes form the vertices of the 4 outer tetrahedrons. We are then left with the four tetrahedrons needed to effectively penalise significant volume compression. A graphical representation of this process is shown in Figures (5.3 - 5.6).

The 4 tetrahedrons associated to node $\mathbf{x}_{ijk}$ are of the following form:

Index	x-vextor (rod)	$\mathbf{d}_y$ vector	$\mathbf{d}_z$ vector
1	$-\mathbf{v}_{ijk}$	$\mathbf{d}_{y(ijk)}$	$\mathbf{d}_{z(ijk)}$
2	$\mathbf{v}_{i(j+1)k}$	$-\mathbf{d}_{y(ij(k-1)}$	$\mathbf{d}_{z(i(j+1)(k-1))}$
3	$\mathbf{v}_{(i+1)jk}$	$\mathbf{d}_{y((i+1)j(k-1))}$	$-\mathbf{d}_{z(ij(k-1))}$
4	$-\mathbf{v}_{(i+1)(j+1)k}$	$-\mathbf{d}_{y(i+1)jk}$	$-\mathbf{d}_{z(i(j+1)k)}$

The advantage of this approach is that tetrahedral volume is very easy to calculate:

$$Vol_{Tet} = \frac{1}{6}|\mathbf{a} \cdot (\mathbf{b} \times \mathbf{c})|, \tag{5.28}$$

and the volume of the undeformed tetrahdrons is

$$Vol_0 = \frac{1}{6} r d_y d_z. \tag{5.29}$$

We impose an energy penalty of the form

$$E_t = \sum_{i=1}^{l-1} \sum_{j=1}^{m-1} \sum_{k=0}^{n} \sum_{s=1}^{4} C_1 e^{-C_2 \frac{Vol_{Tet(s(i,j,k))}}{Vol_0}}, \tag{5.30}$$

where $Vol_{Tet(s(i,j,k))}$ is tetrahedron of index s associated to node $\mathbf{x}_{ijk}$ and C_1, C_2 are sufficiently large to ensure the penalty is negligible for all but the most significant compression.

5.4 Loading Potentials

In this model 3 types of load are considered and both are applied only to the exterior of the bundle.

5.4.1 Lateral Force

N_x is a force applied in the negative x direction to the furthest most nodes: $\mathbf{x}_{ijn}$ in our notation. This force has an energy potential:

$$E_f^x = -N_x r \sum_{i=1}^{l} \sum_{j=1}^{m} \cos\theta_{ijn} \cos\phi_{ijn}, \tag{5.31}$$

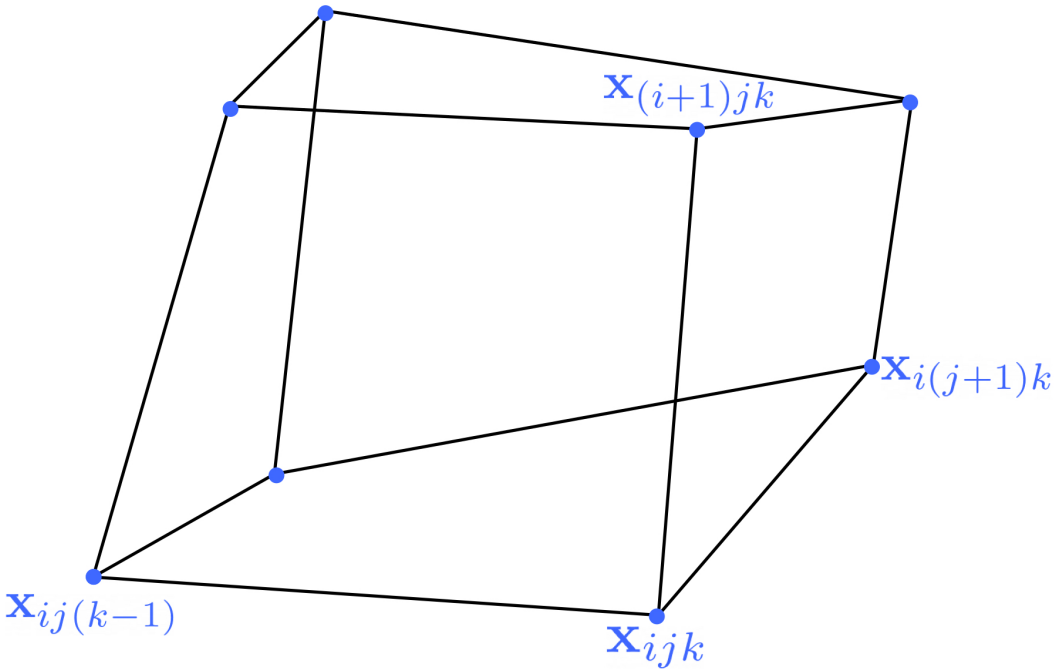

Figure 5.3: The local internal volume

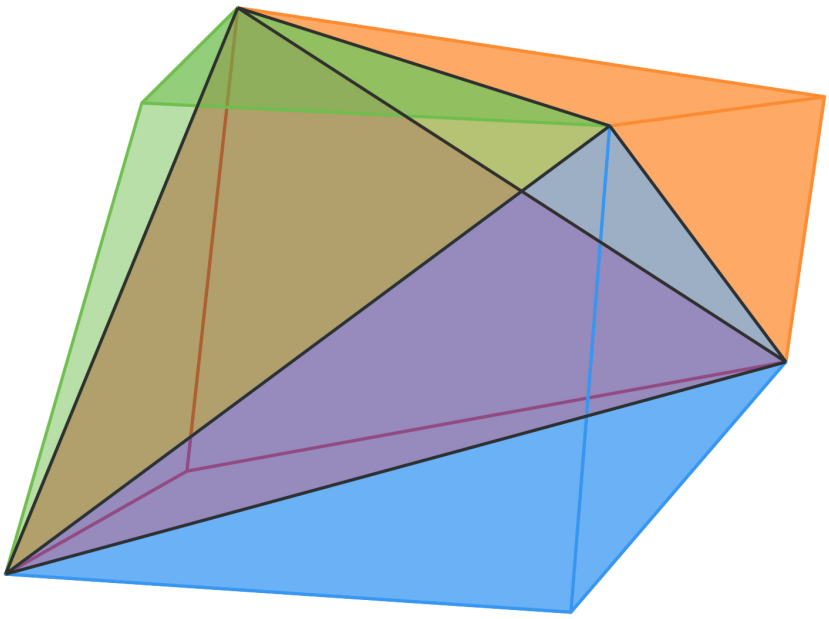

Figure 5.4: Subdivisions into 5 tetrahedrons

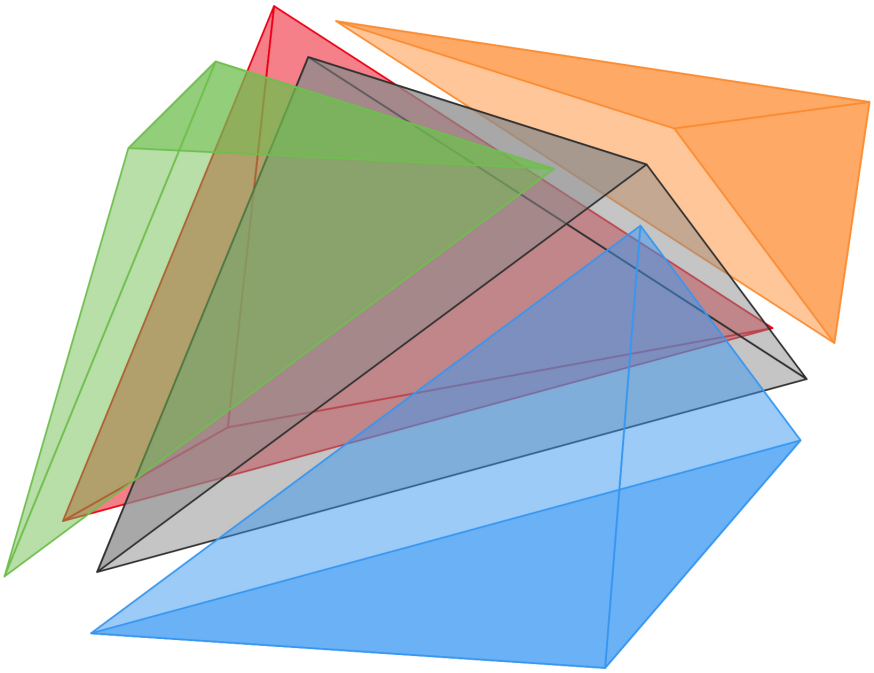

Figure 5.5: We neglect the inner tetrahedron

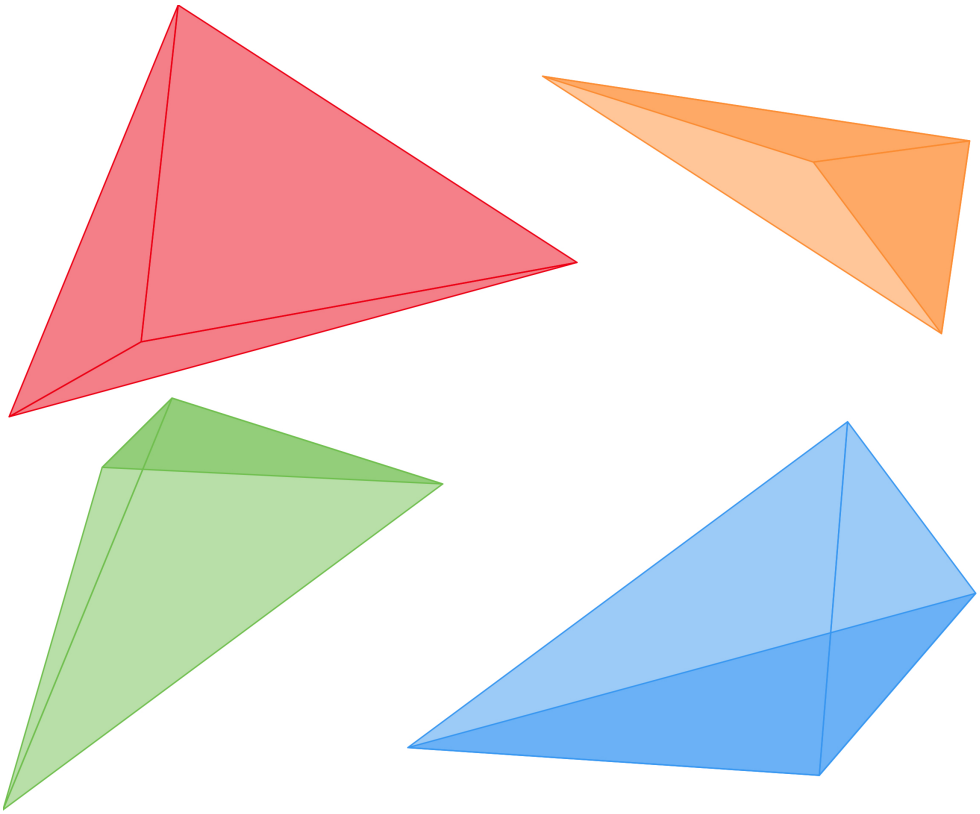

Figure 5.6: The 4 tetrahedrons for which we consider the volume

which sums over the x coordinates of the end-most node of each filament. N_x is modelled as uniform across the bundle.

This load mimics a build up of pressure at one end of a nerve and is particularly applicable to conditions such as glaucoma, in which structural damage to the optic nerve causes a reduction in the visual field [24]. Elevated interocular pressure is considered a major risk-factor for glaucoma and one theory of the association suggests that raised interocular pressure may in turn cause damage in the form of compression of the optic nerve bundle [25][26].

5.4.2 Pinching Force

As axons are the site of electrochemical transmission, compression of a nerve bundle can restrict the axonal transport and have potentially serious structural or functional impacts [27, 28]. To model this phenomena we consider the loads N_y and N_z which are applied uniformly to the exterior of the bundle.

N_y is applied inwards on all filaments of j components 0 and m and has energy potential,

$$E_f^y = N_y r[-\sum_{i=1}^{l}\sum_{k=0}^{n}\sin\theta_{i0k}\cos\phi_{i0k} + \sum_{i=1}^{l}\sum_{k=0}^{n}(\sin\theta_{imk}\cos\phi_{imk} - W)]. \tag{5.32}$$

Similarly, N_z is applied inwards on all filaments of i components 0 and l and has energy potential,

$$E_f^z = N_y r[-\sum_{j=1}^{m}\sum_{k=0}^{n}\sin\phi_{0jk} + \sum_{j=1}^{m}\sum_{k=0}^{n}(\sin\phi_{ljk} - H)]. \tag{5.33}$$

These potentials sum over the distance which the external filaments deform in the direction which they experience pinching. As in the case of N_x, these forces are modelled uniformly across the length of the bundle although there is scope to consider more localised compression to model situations such as entrapment in anatomical tunnels or fluid build up in the epineurium (edema) following traumatic injury [27, 29].

5.4.3 Rotation Force

Since it has always been an aim of this project to explore torsional behaviour, a small angle rotational force which acted on the external boundaries was modelled. This was of the form

$$\begin{aligned} E_{rot} = {} & N_{rot}\sum_{j=1}^{m}\sum_{k=1}^{n}((\sin\theta_{ljk}\cos\phi_{ljk} - \sin\theta_{lj0}\cos\phi_{lj0}) - (\sin\theta_{1jk}\cos\phi_{1jk} - \sin\theta_{1j0}\cos\phi_{1j0})) \\ & + N_{rot}\sum_{i=1}^{l}\sum_{k=1}^{n}((\sin\phi_{i1k} - \sin\phi_{i10}) - (\sin\phi_{imk} - \sin\phi_{im0}))\,. \end{aligned} \tag{5.34}$$

5.5 Boundary Conditions

For this model we imposed both clamped and pinned boundary conditions to be able to model a variety of different biological scenarios.

Pinned Conditions

A pinned body is one which has a fixed position at either end but is able to rotate at that fixed position. To model this scenario we impose a quadratic penalty of the form

$$E_b^p = C_3 \sum_{i=1}^{l} \sum_{j=1}^{m} \left((\sin\theta_{ij0}\cos\phi_{ij0} - \sin\theta_{ijn}\cos\phi_{ijn})^2 + (\sin\phi_{ij0} - \sin\phi_{ijn})^2 \right). \tag{5.35}$$

This penalises horizontal or vertical displacement of the endmost node relative to the position of the $0th$.

Clamped Conditions

A clamped body is one which is unable to rotate around either of its endpoints. To model this scenario we impose a quadratic penalty of the form

$$E_b^c = C_3 \sum_{i=1}^{l} \sum_{j=1}^{m} \left(\theta_{ij0}^2 + \theta_{ijn}^2 + \phi_{ij0}^2 + \phi_{ijn}^2 \right). \tag{5.36}$$

This penalises rotation of the $1st$ and nth filament.

5.6 Non-Dimensionalisation

To generalise the model, we follow the same procedure as [9] and non-dimensionalise based on the width and height (W) of the bundle and a reference bending stiffness $B_{ref} = 0.1$. W has dimensions L while B_{ref} has dimensions ML^3T^{-2}.
The following table includes parameters before and after the non-dimensionalisation procedure.

Parameter	Description	Dimensions	Non-dimensionalised equivalent
L	length	L	$L' = L/W$
W	width	L	$W' = W$
H	height	L	$H' = H/W$
N_x	lateral load in x direction	MLT^{-2}	$N'_x = N_x W^2/B_{ref}$
N_y	pinching load in y direction	MLT^{-2}	$N'_y = N_y W^2/B_{ref}$
N_z	pinching load in z direction	MLT^{-2}	$N'_z = N_z W^2/B_{ref}$
N_{rot}	rotational load	MLT^{-2}	$N'_{rot} = N_{rot} W^2/B_{ref}$
K	spring stiffness	ML^2T^{-2}	$K' = KW/B_{ref}$

As is convention, we now drop the primes and all parameters henceforth can be considered non-dimensionalised.

5.7 Energy Minimisation

Minimal energy states were found using the Limited-memory Broyden–Fletcher–Goldfarb–Shanno (L-BFGS) algorithm, a quasi-Newton method commonly used for non-linear optimisation problems to find the extrema of a scalar function $f(\mathbf{x})$. In this case the scalar function f is

the energy function and the vector $\mathbf{x}$ is the ordered angles which parameterise the positions of nodes in the system.

$$\mathbf{x} = (\theta_{110}, ...\theta_{lmn}, \phi_{110}...\phi_{lmn}) \tag{5.37}$$

Newton's method requires a calculation of the inverse Hessian - H - for each iteration which is typically computationally costly but the BFGS algorithm approximates H directly using successive gradient vectors. The L-BFGS further reduces the computational load by reducing the amount of information stored. While the BFGS stores a full $N \times N$ approximation of the Hessian, in this case $2lm \times 2lmn$ the L-BFGS instead stores a few vectors which implicitly describe the problem [30].

A random list of $2lmn$ angles are generated with magnitude ≤ 0.05 as the initial parameters of the energy function which are then used to define the initial positions of each node according to 4.4. The rms-convergence rate for this model was set to 10^{-5}.

A full derivation of the gradient of bending energy, interaction energy and non-overlap penalty with respect to the angles θ_{ijk}, ϕ_{ijk} is contained in Appendix A.

Chapter 6

Results

It is worth noting that while this model was effective at simulating a range of qualitative behaviours, these were very difficult to analyse quantitatively and the length of time that simulations took to complete - a set of 80 simulations took 12 days and another set of 3 took 36 hours - meant that parameter ranges had larger intervals than would normally be desirable to analyse the transitional behaviour of bundles between stable modes. Unless otherwise specified, the material parameters of the bundle are as such:

- $B_{int} = 0.01$
- $B_{ext} = 0.1$
- $K = 0.0001$

Due to the complexity of the model, it is only possible to consider a few of the qualitative dynamic behaviours which were exhibited when external parameters were chosen. Specifically, the decision was made to focus on pinching, buckling and rotation. The understanding of pinching is relatively intuitive as the external boundary deforming inwards and can be seen below.

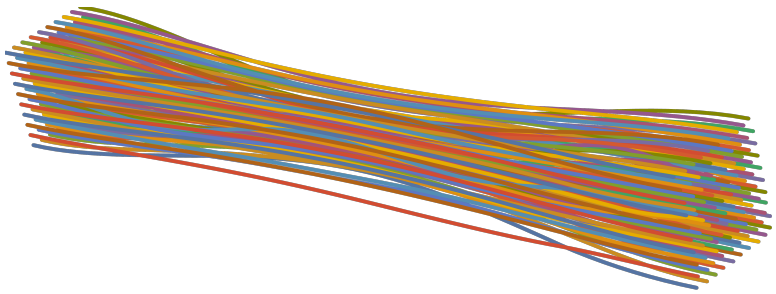

Figure 6.1: Pinched configuration, Nx = 0, Ny = 0.0625, Nz = 0.0625

6.1 Buckling

The notion of buckling is that of a rapid deformation under a critical load. Broadly, here we consider buckling to be behaviour which opposes a lateral force by reducing the length of the bundle when projected along the direction parallel to the applied load - here the x axis. Buckling behaviour is typically exhibited upon application of a critical load.

In the planar model, upon application of an increasing lateral load the bundle would exhibit either internal or global buckling where internal buckling was localised buckling behaviour with little to no deformation of the outer boundary and global buckling was a symmetric buckling of the whole bundle. Two examples of this behaviour both from [9] are shown below. The determining factor in which behaviour occurred was the ratio of the external to internal bending coefficient B_{RAT}. In clamped conditions as are investigated here, it was broadly true that for a sufficiently large lateral load, bundles would buckle globally for $B_{RAT} < 100$ and internally for $B_{RAT} \geq 100$. This makes sense, the stiffer the external boundary, the more resistant it is to deformation under external loading and so the less likely it is to buckle.

However, in this model, the behaviour looks very different. B_{RAT} is fixed at 10 but global style buckling as seen in the planar model was not observed. Instead behaviour generally fell into 3 categories upon increasing external load - no buckling, internal buckling and finally "breakthrough buckling". The latter two shall be examined further.

6.1.1 Internal Buckling

Internal buckling like behaviour was observed very frequently for lateral loads and was generally characterised by regions of high density bunching while the external filaments showed very little deformation as seen in Figures (6.4). These points of high density were generally concentrated on the edge of the bundle and filaments buckled towards these points. As the load increased further, these points of bunching became more pronounced and densely packed with surrounding filaments buckling in the same direction. Eventually these areas of localosed buckling began to press into the exterior wall. This phenomenon can be observed in Figure (6.5) and is the subject of next section.

A quick note on the boundary

In the planar model, the stiff outer boundary was comprised of the 2 rods at the top and bottom of the bundle. Looking at 6.2 and 6.3, it is not hard to see that self intersection would be required for internal filaments to extend beyond the wall of the bundle. The same is not true for this model. While the non-overlap penalty does prevent local self-intersection, there is currently no explicit energy consideration to prevent internal filaments from slipping through the gaps of the boundary. Obviously, this can't happen in real life as the outer filaments represent a solid boundary and stuff cannot generally just move through walls - AntMan in the quantum realm excluded.

6.1.2 "Breakthrough Buckling"

In the planar model, deformation of the external filaments under buckling was characterised by both external filaments buckling in the same direction. It is possible that such a behaviour would still arise in the 3-dimensional model although the range of parameters of loading potential used was likely not large enough to cause this behaviour to be exhibited. What was observed however was localised buckling of the external filaments while the rest were largely undeformed as seen in Figures(6.5 and 6.6. This has here been defined as "breakthrough buckling" and is characterised by localised external filament buckling.

The fact that internal buckling was always observed before breakthrough buckling gives rise to the suggestion that global buckling in a filament bundle with a significantly less elastic boundary could be partially initiated by a localised internal region of high pressure

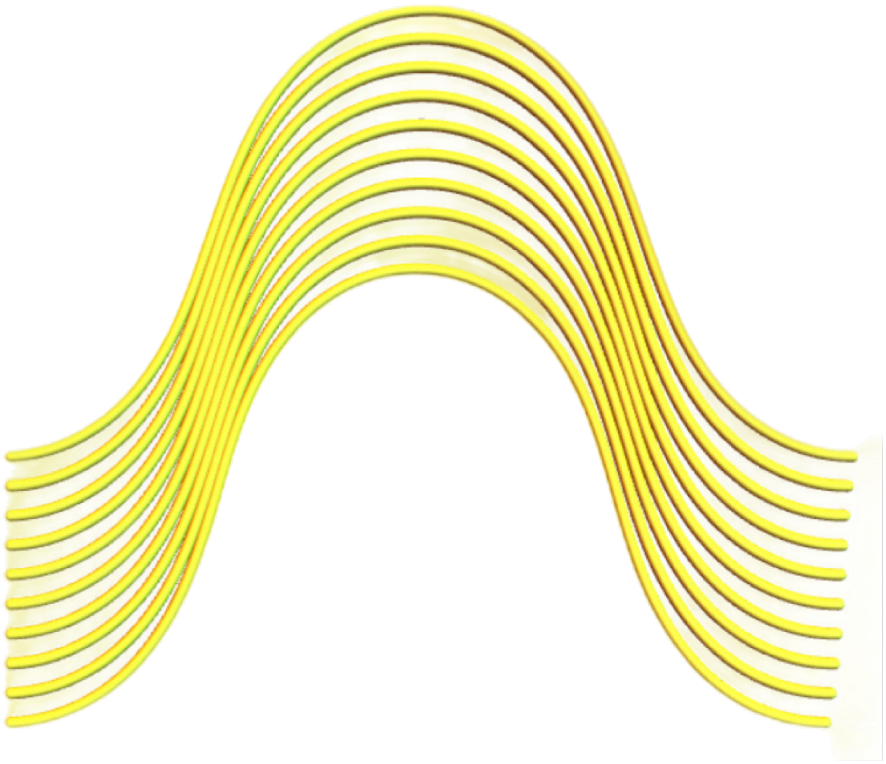

Figure 6.2: Planar global buckling

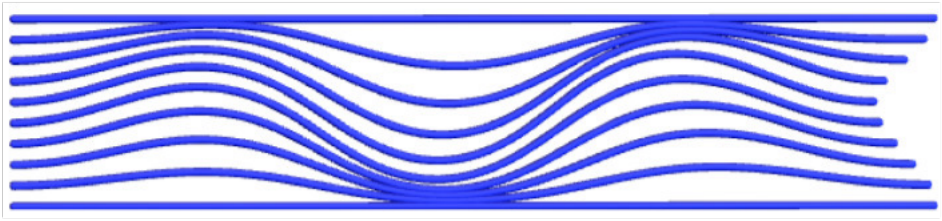

Figure 6.3: Planar internal buckling

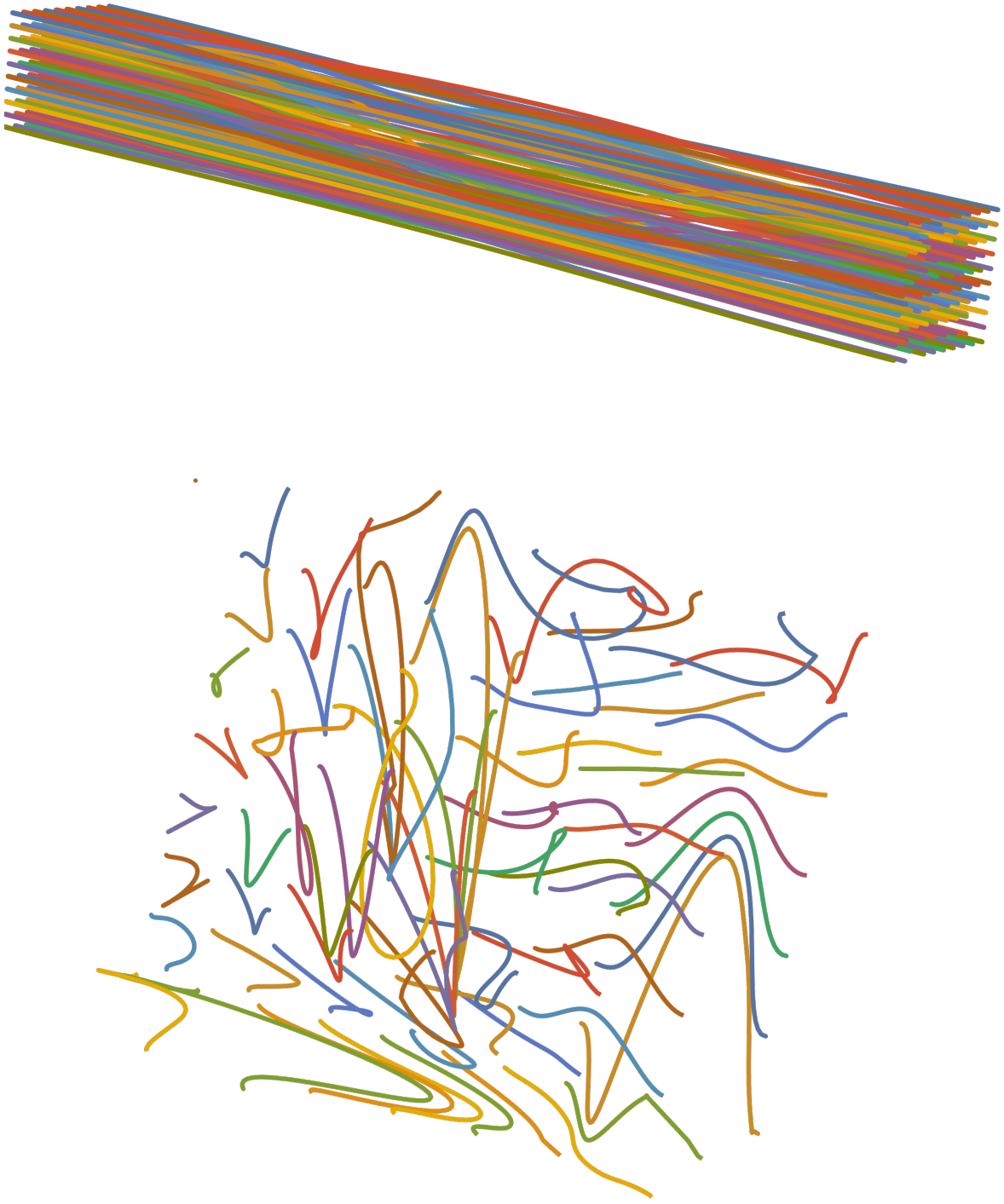

Figure 6.4: The side and end view of an internally buckled configuration - the outer filaments are excluded in the end view. Nx = 0.1875, Ny = 0.00625, Nz = 0.00625

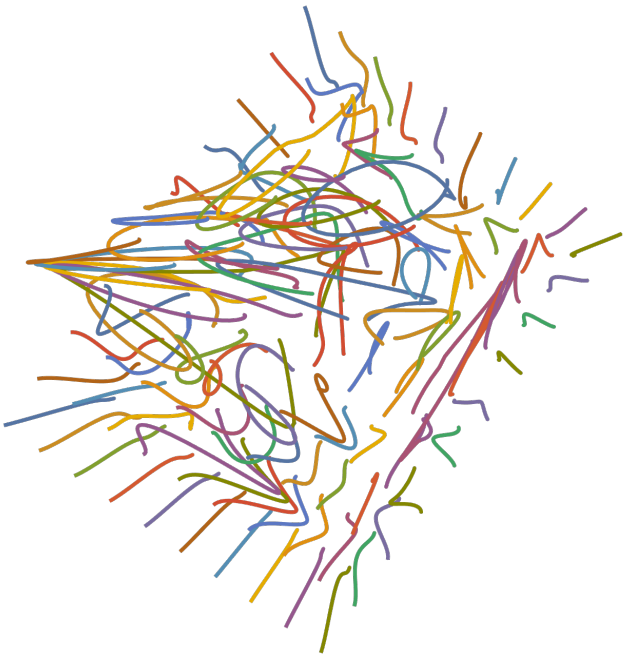

Figure 6.5: Nx = 0.5, Ny = 0.00625, Nz = 0.00625

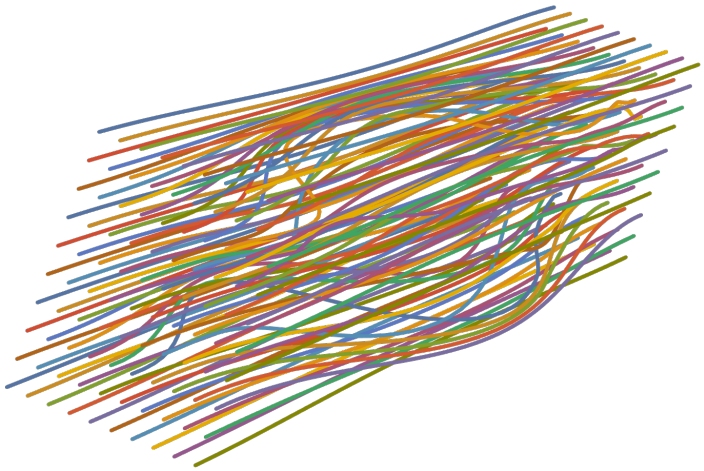

Figure 6.6: Nx = 0.5625, Ny = 0.00625, Nz = 0.00625

causing the external boundary to buckle outwards as well as being a macroscopic response by the whole bundle to external lateral loading.

The challenge of verifying this using the model outlined here is that each new simulation of the model has random initial angles. While similar types of qualitative behaviour will be observed for each simulation with the same input parameters, the locations of these high pressure regions along the boundary will differ. It is therefore not possible to associate model outputs to one another or study the transition between specific simulations beyond observing the changes in type of qualitative behaviour exhibited.

A potential solution to this problem would be to define a range of lateral loads and then apply subsequent loads iteratively, using the minimal energy configuration under the previous load as the starting configuration. This would allow simulations to be associated to one another and could be used to check this theory.

6.2 Rotation

Initially, the modelling choice was made to remove the penalty on the n^{th} nodes deviating from their x position - the pinched condition - and instead only impose a penalty on deviation from an endpoint orientation of $\theta_{ijn} = 0, \phi_{ijn} = 0$. This was to allow for behaviour whereby one end of the bundle could rotate. This had some initially positive results as shown in the Figures (6.7 - 6.9) where rotation is clearly visible.

The challenge however, was that upon application of higher rotational loads, the removal of the pinned conditions caused significant divergence of the filaments at the end point, as shown in Figures (6.10 and 6.11).

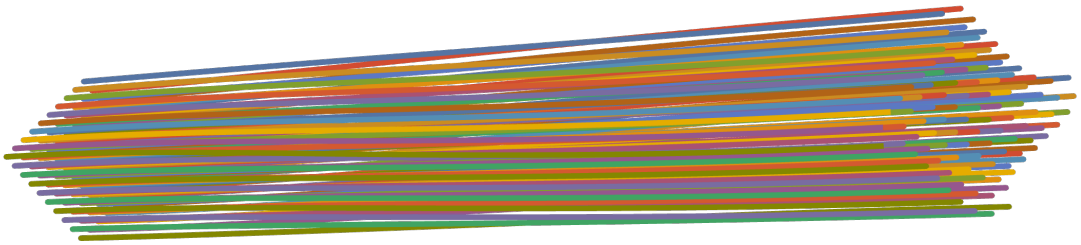

Figure 6.7: Nrot = 0.00625

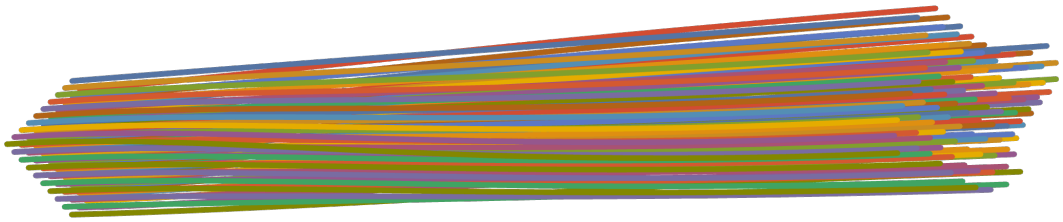

Figure 6.8: Nrot = 0.0125

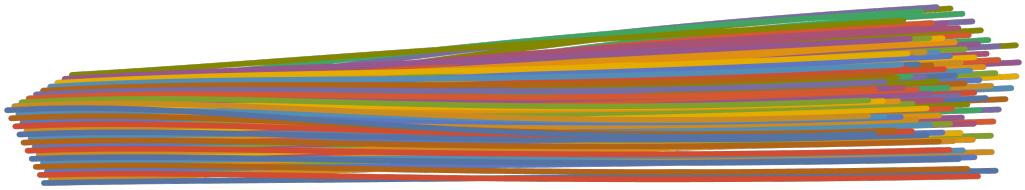

Figure 6.9: Nrot = 0.01875

2 approaches were then taken to address this divergent behaviour. One was to reimpose the clamped boundary conditions and the other was to increase the spring coefficient which had been kept constant at 0.0001 for all previous runs under varying volume and direction of loading.

Increasing the spring coefficient had a positive effect in this area as can be seen in the comparison between Figures (6.11 and 6.12). The globally helical shape formed by the bundle is one which has significant scope to study further. Other further research could include studying the effect of applying both lateral and rotational loads.

6.3 Computational Limitations

6.3.1 Parameter variations

The sheer number of possible parameter variations makes it almost impossible to analyse all behaviours exhibited by model configurations. While an effort has been made to focus on 3 particular qualitative behaviours, a modelling choice was made to keep system parameters - bending coefficients, spring constant, penalty coefficients and the ratio of the internal to external bending coefficients constant. This reduced the possible number of parameters significantly and simplified the analysis of results to looking solely at the impact of externally

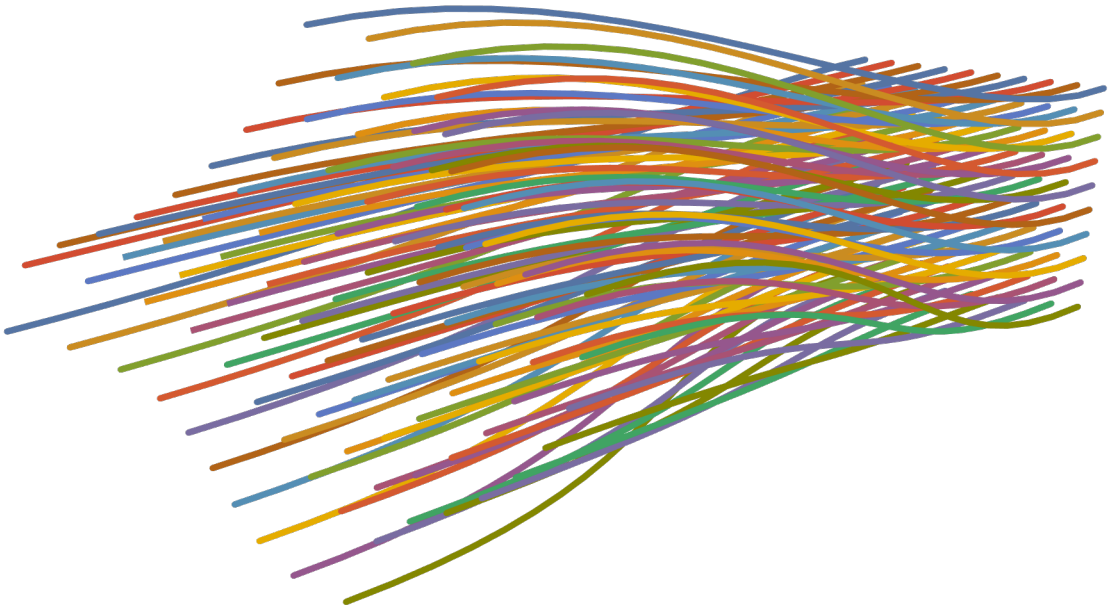

Figure 6.10: Nrot = 0.025

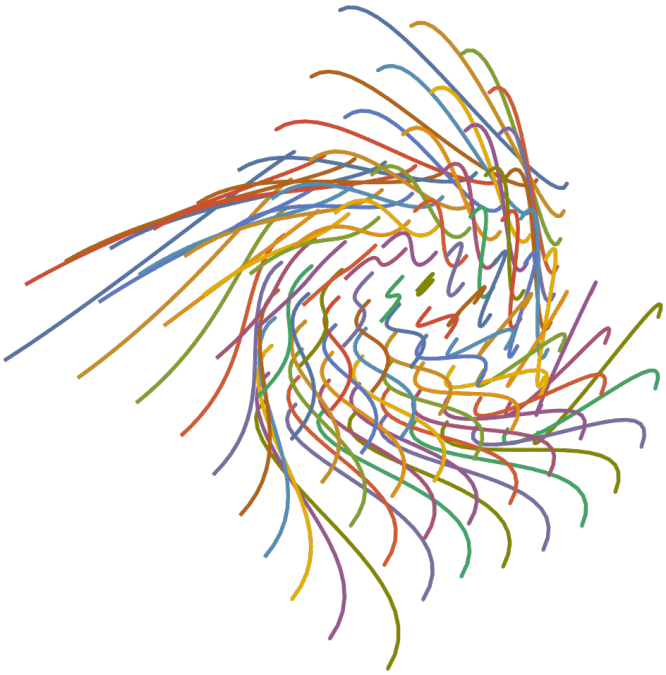

Figure 6.11: Divergence of the end points

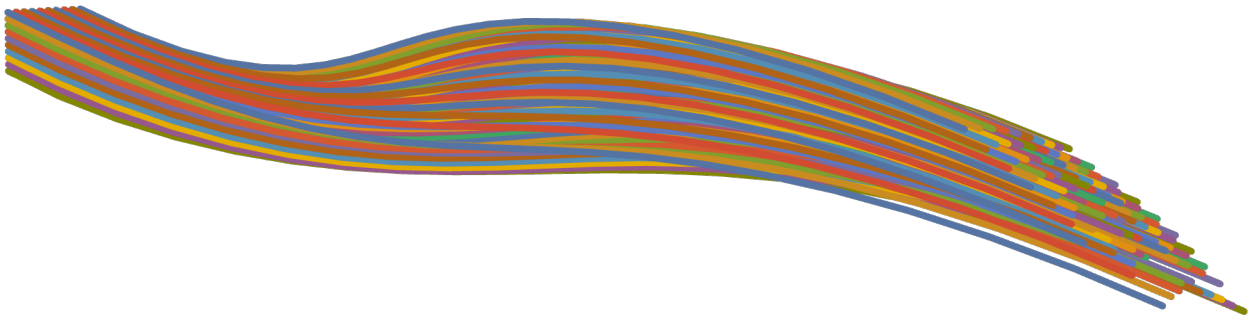

Figure 6.12: K = 0.001, $N_{rot} = 0.025$

applied forces. There is however, significant scope to examine further the impact of varying system constants.

6.3.2 Outer Boundary

One particular phenomenon which has proved very very difficult to prevent and as such has actually not been tackled in this paper is that of making the outer boundary sufficiently solid that interior filaments cannot slip through and extend beyond the boudnaries of the bundle. While the non-overlap penalty is highly effective at preventing self intersection, the outer boundary is just a collection of filaments with gaps between them and so internal filaments can move through the gaps without intersecting.

A solution to this problem would require the modelling of a 2 dimensional outer boundary layer and then a different self-intersection detection algorithm would be needed.

Chapter 7

Axially Symmetric Model

Since this research was the extension of a planar model, for simplicity it was appropriate to initially consider a cartesian system. Here, the undeformed structure had filaments arranged as described in 4.3.

However, during the process of analysing the results it became clear that this choice of geometry, specifically that the shape of the stiff boundary layer caused breakthrough buckling to be concentrated in the corners. It was therefore appropriate to derive a new model which gave no directional bias to internal buckling. As such an axially symmetric model was designed.

7.1 The Set Up

To minimise the need for large scale changes to the code, the choice was made to retain the structure of a collection of chains of filaments indexed over 3 dimensions R, α, z. In this way the position of nodes of $\mathbf{x}_{ijk}$, for $k \geq 1$ relative to $\mathbf{x}_{ij0}$ as shown in 4.4 is retained, what was changed was the initial positions of nodes $\mathbf{x}_{ij0}$. Crucially, this means that much of the mathematics does not change as the properties of individual filaments has not changed, merely their position in an undeformed configuration.

m is now the number of filaments of fixed R while l the number of radial rings. For a model indexed over the 3 coordinates (R, α, z) with radius Rad the initial nodes were as follows.

$$\mathbf{x}_{ij0} = (0, R\cos(\alpha), R\sin(\alpha)) \tag{7.1}$$

where

$$R = i\frac{Rad}{l} \tag{7.2}$$

$$\alpha = (j-1)\frac{2\pi}{m} \tag{7.3}$$

as shown in 7.1

Broadly, the same energy considerations were taken for the axially symmetric model and the previous model - now known as the Cartesian model - with the exception of rotational loading. There was no change to the energy formulations for bending, lateral loading or imposition of boundary conditions.

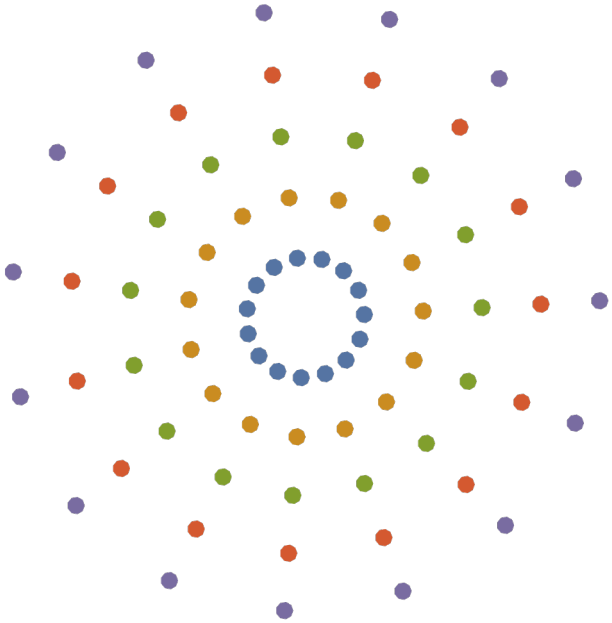

Figure 7.1: The initial positions of nodes in the ASM

7.2 Energy Considerations

Bending

Since bending energy does not take into account the position of a filament in space or its interaction with other filaments, the formulation is independent of the initial configuration of the structure and as such 5.1 is applicable to this model. The only difference was that the stiff outer sheath was modelled by having a uniform bending stiffness for $i < l$ with a higher bending stiffness for $i = l$

Lateral Loading

The potential 5.31 can be used here as this relies only on x-direction deformation and is indexed over 2 other dimensions.

Boundary Conditions

The same quadratic boundary conditions were imposed as described in 5.5. Since no rotational forces were applied, there was no need to remove the condition on position as was necessary in the Cartesian model.

7.2.1 Interaction Energy

We still model the interaction between adjacent filaments using the Hookean potentials outlined in Section 5.2 and again consider both straight and diagonal springs with uniform

spring constant

$$f(d_{r(ijk)}) = \frac{K}{2}\left(\frac{d_{r(ijk)} - d_r}{d_r}\right)^2 \tag{7.4}$$

$$f(d_{\alpha(ijk)}) = \frac{K}{2}\left(\frac{d_{\alpha(ijk)} - d_{\alpha(i)}}{d_{\alpha(i)}}\right)^2 \tag{7.5}$$

$$f(d^{\pm}_{r(ijk)}) = \frac{K}{2}\left(\frac{d^{\pm}_{r(ijk)} - d^{\pm}_r}{d^{\pm}_r}\right)^2 \tag{7.6}$$

$$f(d^{\pm}_{\alpha(ijk)}) = \frac{K}{2}\left(\frac{d^{\pm}_{\alpha(ijk)} - d^{\pm}_{\alpha(i)}}{d^{\pm}_{\alpha(i)}}\right)^2 \tag{7.7}$$

where,

$$d_{\alpha(ijk)} = \left|\mathbf{d}_{\alpha(ijk)}\right| = \left|\mathbf{x}_{i(j+1)k} - \mathbf{x}_{ijk}\right|, \tag{7.8}$$

$$d_{r(ijk)} = \left|\mathbf{d}_{r(ijk)}\right| = \left|\mathbf{x}_{(i+1)jk} - \mathbf{x}_{ijk}\right|, \tag{7.9}$$

are the straight spring distances and,

$$d^{\pm}_{\alpha(ijk)} = \left|\mathbf{d}^{\pm}_{\alpha(ijk)}\right| = \left|\mathbf{x}_{i(j+1)(k\pm1)} - \mathbf{x}_{ijk}\right|, \tag{7.10}$$

$$d^{\pm}_{r(ijk)} = \left|\mathbf{d}^{\pm}_{r(ijk)}\right| = \left|\mathbf{x}_{(i+1)j(k\pm1)} - \mathbf{x}_{ijk}\right|, \tag{7.11}$$

are the diagonal spring distances.

Note, unlike dy, dz in the cartesian case, the undeformed angular distance $d_{\alpha(i)}$ is not constant throughout the structure but is dependent on i - the radial index,

$$d_{\alpha(i)} = 2i\frac{Rad}{l}\sin\Big(\frac{\pi}{m}\Big). \tag{7.12}$$

The final thing to consider when reformulating the interaction energy was that the structure no longer has 4 external boundaries. It instead only has 2 - due to modelling complexities it was still necessary to consider the lowest i ring to be an external boundary. This meant that , rather than excluding $j = m$, as was done for the cartesian model, the analogue $(d_{\alpha(ijk)})$ and $(d^{\pm}_{\alpha(ijk)})$ are considered for all j.

7.2.2 Pinching Load

Conceptually, this load has a fairly intuitive analogue in the axially symmetric case, and one which is more appropriate for the structures modelled. Instead of 4 different loading forces acting perpendicularly to the outer boundary faces of the bundle as outlined in 5.4.2, this pinching force Nr acts in the radial direction to all filaments for which $i = l$. The energy associated with this load takes the form,

$$\sum_{j=1}^{M}\sum_{k=0}^{N} -N_p(Rad - \sqrt{y^2_{ljk} + z^2_{ljk}}). \tag{7.13}$$

7.2.3 Non-Overlap Penalty

The changes to this energy consideration are similar to those accounted for in the reformulation of interaction energy, particularly that of tetrahedrons being considered for all j rather than excluding $j = m$. Secondly, the initial volume of the tetrahedrons used which is used as a reference for volume compression is no longer constant throughout the structure but is dependent on the radial index i. With $Vol_{0(i)}$ the reference volume of a tetrahedron associated to a point on radial ring i, and with $i \in 1, ..., l-1$ we now have:

$$E_t = \sum_{i=1}^{l-1} \sum_{j=1}^{m-1} \sum_{k=0}^{n} \sum_{s=1}^{4} C_1 e^{-C_2 \frac{Vol_Tet}{Vol_{0(i)}}} \tag{7.14}$$

7.3 Non Dimensionalisation

This follows the same structure as in the Cartesian model with the exception that we use the bundle radius as the reference length. $B_{ref} = 0.01$ which is less than in the Cartesian model. This was changed to reduce the computation time and to increase the range of deformation behaviour observed by making the structure less resistant to deformation.

Parameter	Description	Dimensions	Non-dimensionalised equivalent
L	length	L	$L' = L/W$
Rad	radius	L	$Rad' = Rad$
N_x	lateral load in x direction	MLT^{-2}	$N'_x = NxRad^2/B_{ref}$
N_p	pinching load in radial direction	MLT^{-2}	$N'_p = N_pRad^2/B_{ref}$
K	spring stiffness	ML^2T^{-2}	$K' = KRad/B_{ref}$

7.4 Limitations

While this is a better approximation of the macroscopic dynamics of a cylindrical bundle under loading, due to time constraints it was only possible to consider a model with equal numbers of filaments in each radial layer thus having filaments of higher radial component further apart. Axon packing density varies significantly but this accounts for different tissues - within the same tissue packing density is generally consistent when other structures such as blood vessels and the axonal radius are accounted for [31]. This can be obsered in 1.1. There is evidence that microtubules in axons exhibit locally hexagonal configurations and a reader is directed to [11] for an excellent model of torsion of hexagonaly arranged microtubules. Furthermore, as is briefly eluded to towards the end of 7.2.1 this model treats radial index $i = 1$ as an outer boundary and so does not consider spring potentials or self intersection between filaments of radial index $i = 1$ across the centre of the bundle. In theory this internal space could become highly compressed and local self intersection could occur although that has not yet been observed.

Unfortunately due to the modelling complexity, it was not possible to consider an external rotational force for this model which is a shame since many of the issues which arose when studying the impact of E_{rot} in the cartesian model - particularly around the corners

would have been resolved for a model for which a tangentially applied force would have had less sharp discontinuities.

Chapter 8

Axially Symmetric Results

It is important to note that due to the computational time to run iterations some material parameter adjustments were made for the axially symmetric model. Most significantly, the reference bending coefficient was decreased to 0.01.

8.1 Pinching

As expected, pinched configurations such as those shown in Figure (8.1) behaved similarly to the CB analogue.

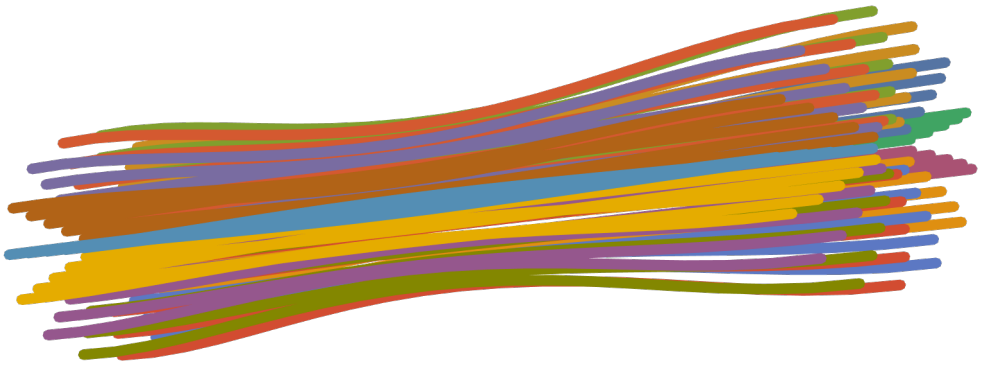

Figure 8.1: A pinched axially symmetric model, Nx = 0.1, Np = 0.2

8.2 Buckling

8.2.1 Internal Buckling

The buckling behaviour of the ASB is again divided into internal and breakthrough buckling. The distinction here in the qualitative behaviour is that the ASB displayed significantly more uniform internal behaviour when both a lateral and pinching load were applied. In the CB, internal buckling generally comprised of multiple areas of bunching which were unevenly distributed throughout the interior and had varied directional bias. In the ASB

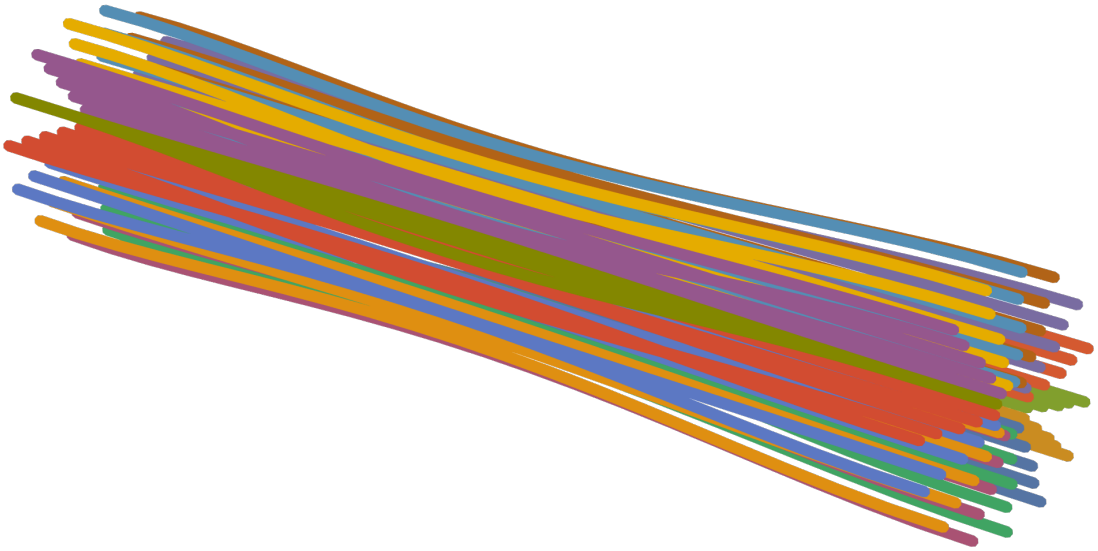

Figure 8.2: The exterior of an axially symmetric bundle which exhibits internal torsion - Nx = 0.4, Np = 0.1

the internal buckling criterion was almost exclusively met by configurations which showed internal filaments buckling in a direction orthogonal to the radius.

As such, it was appropriate to consider a third category of buckling which is only applicable to this model and will henceforth be referred to as torsional buckling. Individual filaments are exhibiting classic Euler buckling but the organised direction of buckling means that globally the bundle exhibits torsion - at least internally.

Figures (8.3 - 8.5) are of a $5 * 15$ ASM which has had a pinching force of 0.1 and a lateral force varying between 0.4 and 0.6. It is worth noting that for $N_x = 0.4$ the torsional buckling inside the structure appears to be organised into rings of alternating direction. The outermost internal ring has buckled radially inwards due to the pinching force but the subsequent internal rings appear to buckle in alternating counter-clockwise and clockwise directions. This is a phenomenon which is not observed for higher lateral loads. Looking at the figures for $N_x = 0.5$ and $N_x = 0.6$ it is clear that torsional buckling occurs in a uniform direction for each model.

An interesting observation was that torsional buckling occured over a much greater range of lateral loada when both a lateral and radial pinching loads were applied; for those bundles which only had a lateral load applied the models were relatively resistant to torsional buckling behaviour. While internal buckling was still observed as an intermediary configuration between no buckling and breakthrough buckling, for these specific configurations, torsional buckling appeared to be a relatively unstable behaviour.

This is an interesting observed property but it is important to note that this is likely to change if a higher exterior bending coefficient is used. The nature of a pinching force significantly increases the energy required for breakthrough buckling to occur since the buckling will occur radially outwards. It is possible therefore that, for these system parameter choices, the exterior bending coefficient is actually too low to materially restrict breakthrough buckling. Instead the pinching force is acting as a pseudo stiff boundary layer.

Figure 8.3: Torsionally buckled ASM - Nx = 0.4, Np = 0.1

8.2.2 Breakthrough Buckling

As eluded to in the analysis of the Cartesian model results the global buckling which was seen in the planar model was not observed in the same way in the 3 dimensional model. The external boundary did deform under large lateral loads but this deformation was localised to regions with high internal pressure. However, the directional bias of breakthrough which was significant in the Cartesian model was no longer present in the ASM.

An attempt was made to try and find the critical lateral load N_x for configurations under pinching force N_p to exhibit breakthrough buckling. This was defined by requiring that at for at least one angular index j, every filament must have a mean radial deformed distance greater than its undeformed radial distance. Unfortunately, this was rarely a strict switch as in the example below which shows the application of an increasing lateral load from 0.61 to 0.64 to a bundle under a pinching load of 0.2. To be able to accurately determine these critical loads it would be necessary to repeat the simulations with the same parameters and calculate a consistency with which the breakthrough buckling behaviour is exhibited. These consistency measurements could be compared and a benchmark tendency defined - the lowest load which achieved the benchmark tendency would be classed as the critical load for that radial pinching force.

Figure 8.4: Torsionally buckled ASM - Nx = 0.5, Np = 0.1

Figure 8.5: Torsionally buckled ASM - Nx = 0.6, Np = 0.1

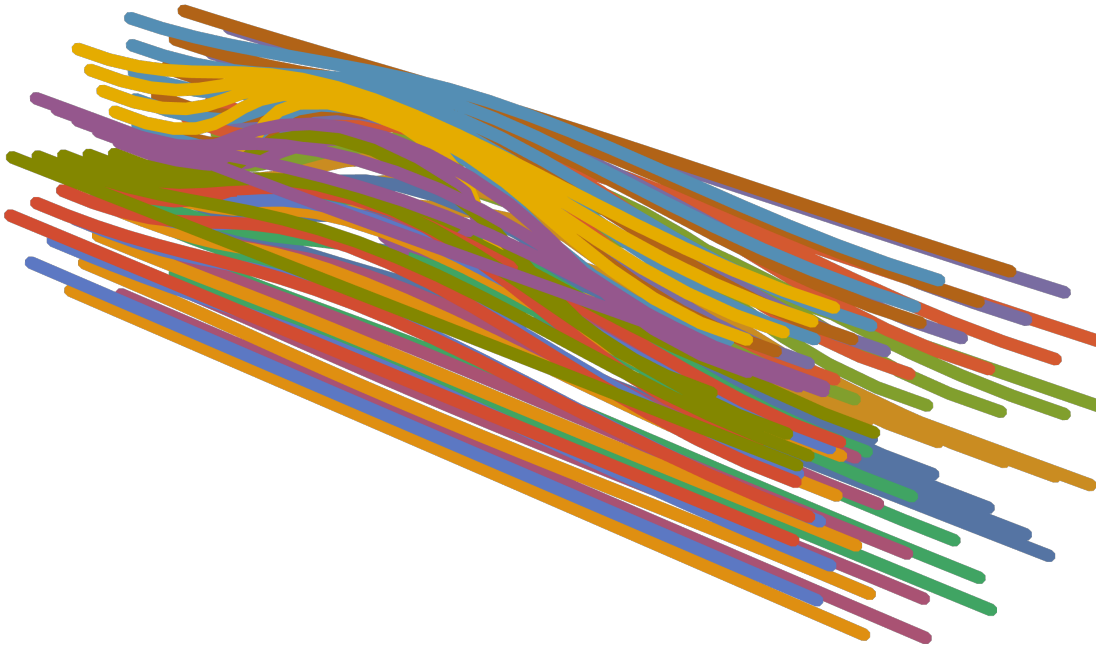

Figure 8.6: A bundle exhibiting breakthrough buckling, $N_x = 0.6, N_p = 0$

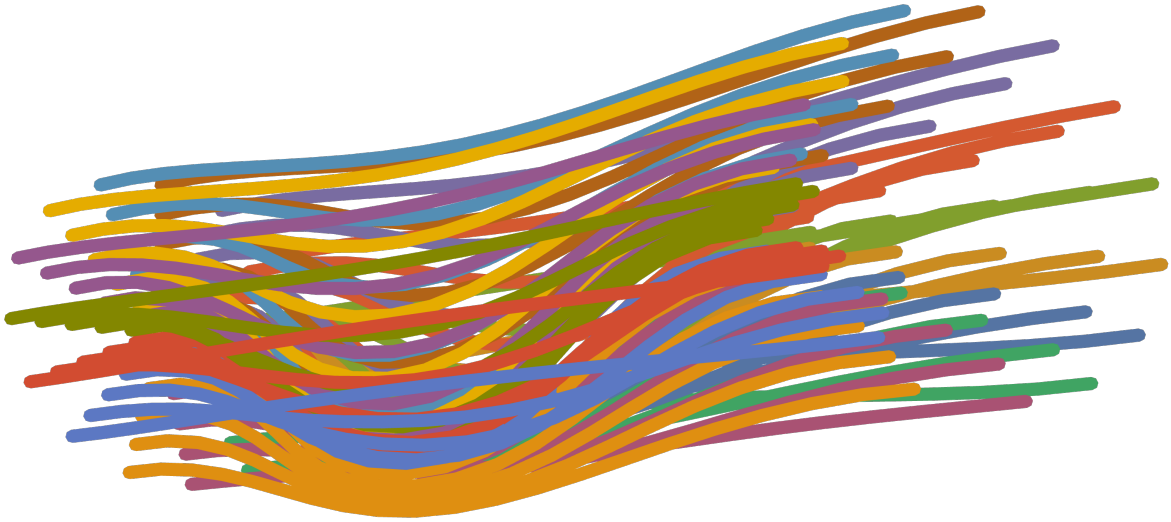

Figure 8.7: A bundle exhibiting breakthrough buckling, $N_x = 0.7, N_p = 0.1$

(a) Nx = 0.61

(b) Nx = 0.62

(a) Nx = 0.63

(b) Nx = 0.64

Chapter 9

Conclusion

9.1 Methodology

The goal of this project was to derive a model to simulate the behaviour of a 3 dimensional bundle of elastic filaments. The model relied on aspects of discrete elastic rod theory and so it was necessary to consider curve theory as well as briefly touching on Kirchhoff Rod Theory before considering the discrete analogues of these theories. The intrinsic energetic considerations were then outlined as well as the range of loads which the model was able to simulate.

Initially, this model had a cuboidal structure with filaments arranged in parallel flat planes but it was realised that this geometric structure exaggerated certain behaviours and suppressed other and so it was necessary to develop a second configuration - that of the axially symmetric model.

9.2 Key Observations and Comparison to the Planar Model

As mentioned in the introduction, this work is an extension of the planar model derived in [9] and as such has heavily drawn on the modelling methodology and the categories outlined in that paper for describing the behaviour of deformed filament bundles. Many of the observed phenomena in the 3-dimensional case are intuitive extensions of the planar case, particularly that of pinching.

However, a key behaviour which was not accounted for in the previous work and has been frequently observed here is that of torsion. Particularly significant was the readiness of an axially symmetric bundle to exhibit internal torsion upon the application of a lateral force when the ability to buckle out radially is restricted. Due to the clinical significance of torsional behaviour in axons, this is an important property to have found.

This work also considers further the mechanics of the transition from internally to globally buckled configurations. While globally buckled states as seen in the planar model were not as readily found, the appearance of breakthrough buckling was a significant phenomenon for thinking about the effect of localised pressure regions caused by internal buckling on the outer boundary. An important theory which will require more research to fully verify is that global buckling is initiated by the outer boundary responding to increased loading from both the external lateral force and from internal regions of localised buckling.

9.3 Further Study

Now the model is functional, there is huge scope to consider the interplay between loading forces and intrinsic parameters. This was something that could not be considered in detail during this project but has significant opportunities for further research. There is also scope to perform more quantitative analysis of critical load values, geometric classification of behaviour and energetics.

Both models require significant development in thinking about how to effectively model the outer boundary as this has proved a significant challenge throughout. With specific regards to the axially symmetric model which is likely to be more useful, this could be further developed to ensure that the packing density is more consistent throughout the structure and rotational loading could be considered.

Appendix A

Energy Function Gradients

These are identical for the cartesian and axially symmetric model with the exception that for the axially symmetric model, intial distances or volumes are dependent in the radial index i.

It is important to also note that here ijk refers to the angle which is being changed where $k \in 1, .., n$. For subsequent affected nodes the indices ijs are are used with $s \in 0, ...n$.

The following partial derivatives will be referred back to repeatedly

$$\frac{\partial \mathbf{x}_{ijs}}{\theta_{ijk}} = \begin{cases} r(-\sin\theta_{ijk}\cos\phi_{ijk}, \cos\theta_{ijk}\cos\phi_{ijk}, 0) & s \geq k \\ 0 \quad \text{otherwise} \end{cases} \tag{A.1}$$

$$\frac{\partial \mathbf{x}_{ijk}}{\phi_{ijk}} = \begin{cases} r(-\cos\theta_{ijk}\sin\phi_{ijk}, -\sin\theta_{ijk}\sin\phi_{ijk}, \cos\phi_{ijk}) & s \geq k \\ 0 \quad \text{othewise} \end{cases} \tag{A.2}$$

The partial derivatives of the energy function considerations with respect to the angles θ_{ijk}, ϕ_{ijk} are as follows

A.1 Bending Energy

For $2 \leq k \leq n-1$

$$\frac{\partial E_b}{\theta_{ijk}} = \frac{2B_{ijk}}{r}\frac{\partial}{\partial\theta_{ijk}}\left(\frac{1-p_{ij(k-1)}}{1+p_{ij(k-1)}} + \frac{1-p_{ijk}}{1+p_{ijk}}\right)$$

$$\frac{\partial E_b}{\phi_{ijk}} = \frac{2B_{ijk}}{r}\frac{\partial}{\partial\phi_{ijk}}\left(\frac{1-p_{ij(k-1)}}{1+p_{ij(k-1)}} + \frac{1-p_{ijk}}{1+p_{ijk}}\right)$$

where $p_{ijk}, p_{ij(k-1)}$ are of the form in 5.2.

$$\begin{aligned}\frac{\partial p_{ijk}}{\theta_{ijk}} &= \frac{1}{r^2}[-\sin\theta_{ijk}\cos\phi_{ijk}\cos\theta_{ij(k+1)}\cos\phi_{ij(k+1)} \\ &+ \cos\theta_{ijk}\cos\phi_{ijk}\sin\theta_{ij(k+1)}\cos\phi_{ij(k+1)}]\end{aligned} \tag{A.3}$$

$$\begin{aligned}\frac{\partial p_{ij(k-1)}}{\theta_{ijk}} &= \frac{1}{r^2}[-\cos\theta_{ij(k-1)}\cos\phi_{ij(k-1)}\sin\theta_{ijk}\cos\phi_{ijk} \\ &+ \sin\theta_{ij(k-1)}\cos\phi_{ij(k-1)}\cos\theta_{ijk}\cos\phi_{ijk}]\end{aligned} \tag{A.4}$$

$$\begin{aligned}\frac{\partial p_{ijk}}{\phi_{ijk}} &= \frac{1}{r^2}[-\cos\theta_{ijk}\sin\phi_{ijk}\cos\theta_{ij(k+1)}\cos\phi_{ij(k+1)} \\ &- \sin\theta_{ijk}\sin\phi_{ijk}\sin\theta_{ij(k+1)}\cos\phi_{ij(k+1)} \\ &+ \cos\phi_{ijk}\sin\phi_{ij(k+1)}]\end{aligned} \tag{A.5}$$

$$\begin{aligned}\frac{\partial p_{ij(k-1)}}{\phi_{ijk}} &= \frac{1}{r^2}[-\cos\theta_{ij(k-1)}\cos\phi_{ij(k-1)}\cos\theta_{ijk}\sin\phi_{ijk} \\ &- \sin\theta_{ij(k-1)}\cos\phi_{ij(k-1)}\sin\theta_{ijk}\sin\phi_{ijk} \\ &+ \sin\phi_{ij(k-1)}\cos\phi_{ijk}]\end{aligned} \tag{A.6}$$

$$\frac{\partial E_b}{\theta_{ijk}} = \frac{-4B_{ijk}}{r}\left(\frac{1}{(1+p_{ij(k-1)})^2}\frac{\partial p_{ij(k-1)}}{\partial\theta_{ijk}} + \frac{1}{(1+p_{ijk})^2}\frac{\partial p_{ijk}}{\partial\theta_{ijk}}\right) \tag{A.7}$$

$$\frac{\partial E_b}{\phi_{ijk}} = \frac{-4B_{ijk}}{r}\left(\frac{1}{(1+p_{ij(k-1)})^2}\frac{\partial p_{ij(k-1)}}{\partial\phi_{ijk}} + \frac{1}{(1+p_{ijk})^2}\frac{\partial p_{ijk}}{\partial\phi_{ijk}}\right) \tag{A.8}$$

For $k = 1$

$$\frac{\partial E_b}{\theta_{ijk}} = \frac{-4B_{ijk}}{r}\left(\frac{1}{(1+p_{ijk})^2}\frac{\partial p_{ijk}}{\partial\theta_{ijk}}\right) \tag{A.9}$$

$$\frac{\partial E_b}{\phi_{ijk}} = \frac{-4B_{ijk}}{r}\left(\frac{1}{(1+p_{ijk})^2}\frac{\partial p_{ijk}}{\partial\phi_{ijk}}\right) \tag{A.10}$$

For $k = n$

$$\frac{\partial E_b}{\theta_{ijk}} = \frac{-4B_{ijk}}{r}\left(\frac{1}{(1+p_{ij(k-1)})^2}\frac{\partial p_{ij(k-1)}}{\partial\theta_{ijk}}\right) \tag{A.11}$$

$$\frac{\partial E_b}{\phi_{ijk}} = \frac{-4B_{ijk}}{r}\left(\frac{1}{(1+p_{ij(k-1)})^2}\frac{\partial p_{ij(k-1)}}{\partial\phi_{ijk}}\right) \tag{A.12}$$

The gradients for the axially symmetric bending energy are identical.

A.2 Interaction Energy

A.2.1 Straight Springs

For $2 \le i \le m-1, 2 \le j \le l-1$

$$\frac{\partial E_s}{\partial\theta_{ijk}} = \sum_{s=0}^{N}\left[\frac{df_{ijs}}{dd_{y(ijs)}}\frac{\partial d_{y(ijs)}}{\partial\theta_{ijk}} + \frac{df_{i(j-1)s}}{dd_{y(i(j-1)s)}}\frac{\partial d_{y(i(j-1)s)}}{\partial\theta_{ijk}} + \frac{df_{ijs}}{dd_{z(ijs)}}\frac{\partial d_{z(ijs)}}{\partial\theta_{ijk}} + \frac{df_{(i-1)js}}{dd_{z((i-1)js)}}\frac{\partial d_{z((i-1)js)}}{\partial\theta_{ijk}}\right]$$

$$\frac{\partial E_s}{\partial\phi_{ijk}} = \sum_{s=0}^{N}\left[\frac{df_{ijs}}{dd_{y(ijs)}}\frac{\partial d_{y(ijs)}}{\partial\phi_{ijk}} + \frac{df_{i(j-1)s}}{dd_{y(i(j-1)s)}}\frac{\partial d_{y(i(j-1)s)}}{\partial\phi_{ijk}} + \frac{df_{ijs}}{dd_{z(ijs)}}\frac{\partial d_{z(ijs)}}{\partial\phi_{ijk}} + \frac{df_{(i-1)js}}{dd_{z((i-1)js)}}\frac{\partial d_{z((i-1)js)}}{\partial\phi_{ijk}}\right]$$

where the total derivative terms are simply

$$\begin{aligned}
\frac{df_{ijs}}{dd_{y(ijs)}} &= \frac{K}{d_y^2}(d_{y(ijs)} - d_y) \\
\frac{df_{ijs}}{dd_{z(ijs)}} &= \frac{K}{d_z^2}(d_{z(ijs)} - d_z) \\
\frac{df_{i(j-1)s}}{dd_{y(i(j-1)s)}} &= \frac{K}{d_y^2}(d_{y(i(j-1)s)} - d_y) \\
\frac{df_{(i-1)js}}{dd_{z((i-1)js)}} &= \frac{K}{d_z^2}(d_{z((i-1)js)} - d_z)
\end{aligned} \tag{A.13}$$

An illustrative example of the derivation of the partial derivatives for $d_{y(ijk)}$ and $d_{y(i(j-1)k)}$ with respect to θ_{ijk} are shown below.

$$\begin{aligned}
d_{y(ijs)} &= \left|\mathbf{d}_{y(ijs)}\right| \\
&= \left|\mathbf{x}_{i(j+1)s} - \mathbf{x}_{ijs}\right| \\
&= \sqrt{(\mathbf{x}_{i(j+1)s} - \mathbf{x}_{ijs}) \cdot (\mathbf{x}_{i(j+1)s} - \mathbf{x}_{ijs})} \\
\frac{\partial d_{y(ijs)}}{\partial \theta_{ijk}} &= \frac{2\left(\frac{-\partial \mathbf{x}_{ijs}}{\partial \theta_{ijk}} \cdot (\mathbf{x}_{i(j+1)s} - \mathbf{x}_{ijs})\right)}{2\sqrt{(\mathbf{x}_{i(j+1)s} - \mathbf{x}_{ijs}) \cdot (\mathbf{x}_{i(j+1)s} - \mathbf{x}_{ijs})}} \\
&= \frac{-1}{d_{y(ijs)}}\left(\mathbf{d}_{y(ijs)} \cdot \frac{\partial \mathbf{x}_{ijs}}{\partial \theta_{ijk}}\right)
\end{aligned} \tag{A.14}$$

$$\begin{aligned}
d_{y(i(j-1)s)} &= \left|\mathbf{d}_{y(i(j-1)s)}\right| \\
&= \left|\mathbf{x}_{ijs} - \mathbf{x}_{i(j-1)s}\right| \\
&= \sqrt{(\mathbf{x}_{ijs} - \mathbf{x}_{i(j-1)s}) \cdot (\mathbf{x}_{ijs} - \mathbf{x}_{i(j-1)s})} \\
\frac{\partial d_{y(i(j-1)s)}}{\partial \theta_{ijk}} &= \frac{2\left(\frac{\partial \mathbf{x}_{ijs}}{\partial \theta_{ijk}} \cdot (\mathbf{x}_{ijs} - \mathbf{x}_{i(j-1)s})\right)}{2\sqrt{(\mathbf{x}_{ijs} - \mathbf{x}_{i(j-1)s}) \cdot (\mathbf{x}_{ijs} - \mathbf{x}_{i(j-1)s})}} \\
&= \frac{1}{d_{y(i(j-1)s)}}\left(\mathbf{d}_{y(i(j-1)s)} \cdot \frac{\partial \mathbf{x}_{ijs}}{\partial \theta_{ijk}}\right)
\end{aligned} \tag{A.15}$$

The $d_{z(ijk)}$ and $d_{z((i-1)jk)}$ derivatives as well as those with respect to ϕ_{ijk} follow trivially.

For $j = 1$ the contributions from $f_{i(j-1)s}$ and $d_{y(i(j-1)s)}$ are ignored and similarly for $i = 1$ the contributions from $f_{(i-1)js}$ and $d_{z((i-1)js)}$ are ignored. Conversely for $j = m$ or $i = l$ we exclude the contributions from f_{ijs} and $d_{y(ijs)}$ or $d_{z(ijs)}$ accordingly.

A.2.2 Diagonal Springs

$$\frac{\partial E_s^+}{\partial \theta_{ijk}} = \sum_{s=0}^{n-1} \left[\frac{df_{ijs}}{dd^+_{y(ijs)}} \frac{\partial d^+_{y(ijs)}}{\partial \theta_{ijk}} + \frac{df_{ijs}}{dd^+_{z(ijs)}} \frac{\partial d^+_{z(ijs)}}{\partial \theta_{ijk}} \right] \tag{A.16}$$

$$+ \sum_{s=1}^{n} \left[\frac{df_{i(j-1)(s-1)}}{dd^+_{y(i(j-1)(s-1))}} \frac{\partial d^+_{y(i(j-1)(s-1))}}{\partial \theta_{ijk}} + \frac{df_{(i-1)j(s-1)}}{dd^+_{z((i-1)j(s-1))}} \frac{\partial d^+_{z((i-1)j(s-1))}}{\partial \theta_{ijk}} \right] \tag{A.17}$$

$$\frac{\partial E_s^-}{\partial \theta_{ijk}} = \sum_{s=1}^{n} \left[\frac{df_{ijs}}{dd^-_{y(ijs)}} \frac{\partial d^-_{y(ijs)}}{\partial \theta_{ijk}} + \frac{df_{ijs}}{dd^-_{z(ijs)}} \frac{\partial d^-_{z(ijs)}}{\partial \theta_{ijk}} \right] \tag{A.18}$$

$$+ \sum_{s=0}^{n-1} \left[\frac{df_{i(j-1)(s+1)}}{dd^-_{y(i(j-1)(s+1))}} \frac{\partial d^-_{y(i(j-1)(s+1))}}{\partial \theta_{ijk}} + \frac{df_{(i-1)j(s+1)}}{dd^-_{z((i-1)j(s+1))}} \frac{\partial d^-_{z((i-1)j(s+1))}}{\partial \theta_{ijk}} \right] \tag{A.19}$$

The partial derivatives with respect to the angles are of the same form as those outlined for the straight section.

A.3 Non-Overlap Penalty

The details of this section are particularly fiddly and a reader is encouraged to look to the included figures for the most intuitive understanding of this derivation.

As shown in Figures (5.3 - 5.6) the non-overlap energy penalty is taken by associating each node (with the exclusion of nodes of index $i = l, j = m,$ or $k = 0$) with 4 tetrahedrons. For the derivatives, we reconsider the way nodes are associated to tetrahedrons as shown in the difference between Figures(A.1) and (A.2). The difference here is that all 4 tetrahedrons' "central node" - the one from which we consider the 3 defining edges to point away from - is $\mathbf{x}_{ijs}$. Computationally, this means that rather than $(l-1)*(m-1)*n$ nodes being associated to 4 tetrahedrons, this new configuration initially associates every point to 4 tetrahedrons and then appropriately excludes those which are invalid.

Within this configuration of the structure we then have to consider all tetrahedrons which have an edge for which $\mathbf{x}_{ijs}, s \geq k$ is one of the nodes. Remembering that $\mathbf{v}_{ijs} = \left|\mathbf{x}_{ijs} - \mathbf{x}_{ij(s-1)}\right|$, these possible edges are:

- $\pm\mathbf{v}_{ijs}$
- $\pm\mathbf{v}_{ij(s+1)}$
- $\pm\mathbf{d}_{y(ijs)}$
- $\pm\mathbf{d}_{y(i(j-1)s)}$
- $\pm\mathbf{d}_{z(ijs)}$
- $\pm\mathbf{d}_{z((i-1)js)}$

For each $\mathbf{x}_{ijs}$ there are 12 tetrahedrons associated to a point of index s which are dependent on angles θ_{ijk}, ϕ_{ijk} as shown in A.3.

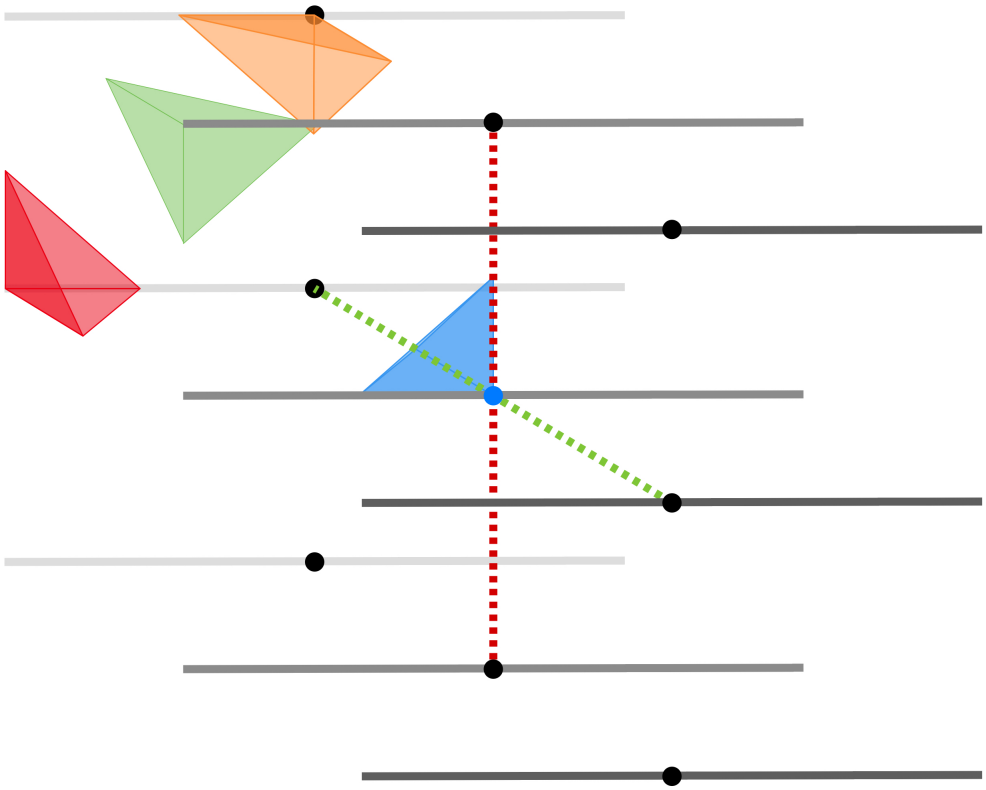

Figure A.1: The assignment of 4 tetrahedrons to a point x_{ijk} (blue) as described in the energy functional

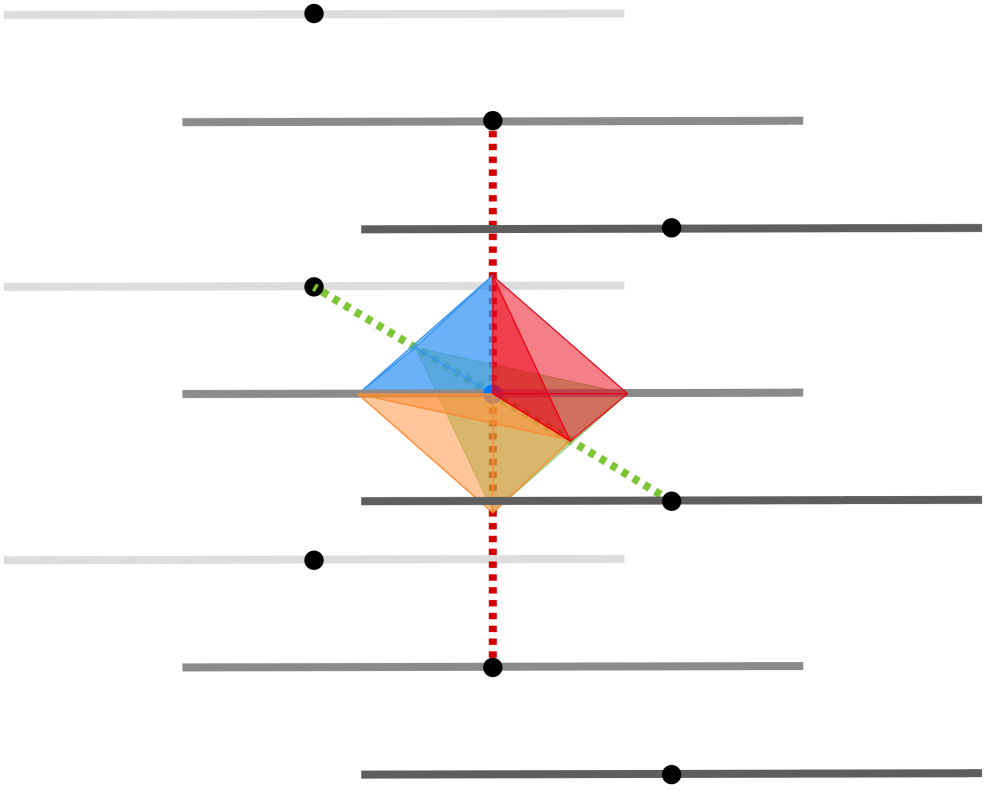

Figure A.2: The assignment of 4 tetrahedrons to a point x_{ijk} (blue) as considered in the energy derivatives

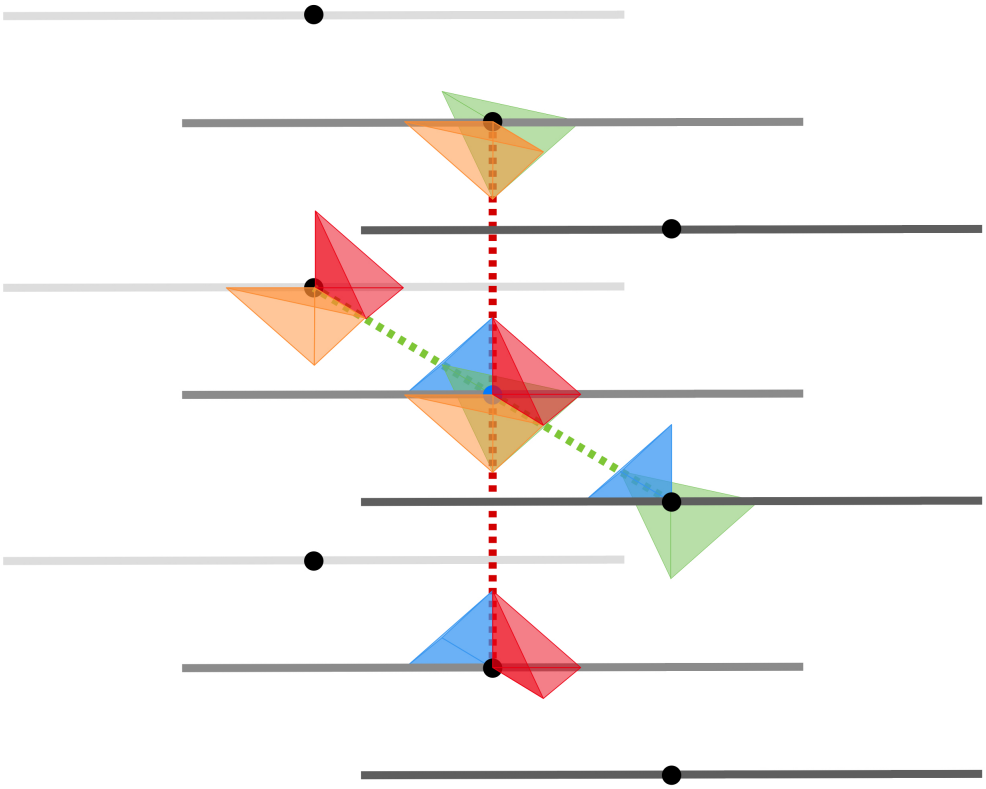

Figure A.3: The 12 tetrahedrons which are associated to a noe x_{ijs} which is dependent on angles θ_{ijk}, ϕ_{ijk}

In illustrative example is given for the gradient of the exponential function with one term of the non-overlap penalty.

$$\frac{\partial}{\partial \theta_{ijk}} \left(C_1 e^{-C_2 \frac{Vol_{Tet}}{Vol_0}} \right) = -\frac{C_1 C_2}{Vol_{Tet(s(ijk))}} \frac{\partial Vol_{Tet(s(ijk))}}{\partial \theta_{ijk}} e^{\frac{-C_2}{Vol_0}} \tag{A.20}$$

Where

$$\frac{\partial Vol_{Tet(s(ijk))}}{\partial \theta_{ijk}} = \frac{1}{6} \text{sgn}(\mathbf{a} \cdot (\mathbf{b} \times \mathbf{c})) \left(\frac{\partial \mathbf{a}}{\partial \theta_{ijk}} \cdot (\mathbf{b} \times \mathbf{c}) + \frac{\partial \mathbf{b}}{\partial \theta_{ijk}} \cdot (\mathbf{c} \times \mathbf{a}) + \frac{\partial \mathbf{c}}{\partial \theta_{ijk}} \cdot (\mathbf{a} \times \mathbf{b}) \right). \tag{A.21}$$

The partial derivatives of the vectors are all

$$\pm \frac{\partial \mathbf{x}_{ijs}}{\theta_{ijk}}. \tag{A.22}$$

A.20 is summed over the 12 tetrahedrons associated to each point $\mathbf{x}_{ijs}$.

Appendix B

Derivation of Discrete Curvature

Taking α_i as the internal angle, we can inscribe an osculating circle between $\mathbf{v}_i$ and $\mathbf{v}_{i+1}$ Bisecting α we now have

$$\tan\Big(\frac{\alpha_i}{2}\Big) = \frac{R_i}{\frac{1}{2}} \tag{B.1}$$

$$= 2R_i \tag{B.2}$$

$$\alpha_i = \arccos(-p_i) \tag{B.3}$$

$$\frac{\alpha_i}{2} = \frac{1}{2}\arccos(-p_i) \tag{B.4}$$

Using the standard half-angle formula (B.5)

$$\tan\Big(\frac{\alpha_i}{2}\Big) = \frac{1-\cos(\alpha_i)}{\sin(\alpha_i)} \tag{B.6}$$

$$\cos(\arccos(-p_i)) = -p_i \tag{B.7}$$

$$\sin(\arccos(-p_i)) = \sqrt{1-p_i^2} \tag{B.8}$$

$$\tan\Big(\frac{\alpha_i}{2}\Big) = \frac{1+p_i}{\sqrt{1-p_i^2}} \tag{B.9}$$

$$2R_i = \frac{1+p_i}{\sqrt{1-p_i^2}} \tag{B.10}$$

$$\frac{1}{R_i} = \kappa_i = \frac{2\sqrt{1-p_i^2}}{1+p_i} \tag{B.11}$$

$$= 2\sqrt{\frac{1-p_i}{1+p_i}} \tag{B.12}$$

Bibliography

[1] G. Cooper and K. Adams, *The cell: a molecular approach*. Oxford University Press, 2022.

[2] A. R. Gillies and R. L. Lieber, "Structure and function of the skeletal muscle extracellular matrix," *Muscle & nerve*, vol. 44, no. 3, pp. 318–331, 2011.

[3] J. D. Stewart, "Peripheral nerve fascicles: anatomy and clinical relevance," *Muscle & nerve*, vol. 28, no. 5, pp. 525–541, 2003.

[4] R. M. Menorca, T. S. Fussell, and J. C. Elfar, "Peripheral nerve trauma: mechanisms of injury and recovery," *Hand clinics*, vol. 29, no. 3, p. 317, 2013.

[5] A. Alizadeh, S. M. Dyck, and S. Karimi-Abdolrezaee, "Traumatic spinal cord injury: an overview of pathophysiology, models and acute injury mechanisms," *Frontiers in neurology*, vol. 10, p. 282, 2019.

[6] A. M. Kabir, D. Inoue, T. Afrin, H. Mayama, K. Sada, A. Kakugo, *et al.*, "Buckling of microtubules on a 2d elastic medium," *Scientific reports*, vol. 5, no. 1, pp. 1–12, 2015.

[7] J. Wu, H. Yuan, and L. Li, "Mathematical modelling of axonal microtubule bundles under dynamic torsion," *Applied Mathematics and Mechanics*, vol. 39, no. 6, pp. 829–844, 2018.

[8] S. J. Peter and M. R. Mofrad, "Computational modeling of axonal microtubule bundles under tension," *Biophysical journal*, vol. 102, no. 4, pp. 749–757, 2012.

[9] C. Prior, J. Panter, and H. Kusumaatmaja, "A minimal model of elastic instabilities in biological filament bundles," *Journal of the Royal Society Interface*, vol. 19, no. 194, 2022.

[10] M. D. Tang-Schomer, A. R. Patel, P. W. Baas, and D. H. Smith, "Mechanical breaking of microtubules in axons during dynamic stretch injury underlies delayed elasticity, microtubule disassembly, and axon degeneration," *The FASEB Journal*, vol. 24, no. 5, pp. 1401–1410, 2010.

[11] C. Lazarus, M. Soheilypour, and M. R. Mofrad, "Torsional behavior of axonal microtubule bundles," *Biophysical journal*, vol. 109, no. 2, pp. 231–239, 2015.

[12] Libretexts, "12.4a: Structure of a nerve," Jan 2023.

[13] L. Woodward and J. Bolton, *A First Course in Differential Geometry: Surfaces in Euclidean Space*. Cambridge University Press, 2019.

[14] E. Abbena, S. Salamon, and A. Gray, *Modern differential geometry of curves and surfaces with Mathematica*. CRC press, 2017.

[15] C. Bär, *Elementary differential geometry*. Cambridge University Press, 2010.

[16] O. M. O'Reilly, *Modeling nonlinear problems in the mechanics of strings and rods*. Springer, 2017.

[17] M. K. Jawed, A. Novelia, and O. M. O'Reilly, *A primer on the kinematics of discrete elastic rods*. Springer, 2018.

[18] M. Bergou, M. Wardetzky, S. Robinson, B. Audoly, and E. Grinspun, "Discrete elastic rods," in *ACM SIGGRAPH 2008 papers*, pp. 1–12, 2008.

[19] A. Travers and J. Thompson, "An introduction to the mechanics of dna," *Philosophical Transactions of the Royal Society of London. Series A: Mathematical, Physical and Engineering Sciences*, vol. 362, no. 1820, pp. 1265–1279, 2004.

[20] F. Bertails, B. Audoly, M.-P. Cani, B. Querleux, F. Leroy, and J.-L. Lévêque, "Super-helices for predicting the dynamics of natural hair," *ACM Transactions on Graphics (TOG)*, vol. 25, no. 3, pp. 1180–1187, 2006.

[21] M. Nizette and A. Goriely, "Towards a classification of euler–kirchhoff filaments," *Journal of mathematical physics*, vol. 40, no. 6, pp. 2830–2866, 1999.

[22] F. Bertails, C. Ménier, and M.-P. Cani, *A practical self-shadowing algorithm for interactive hair animation*. PhD thesis, INRIA, 2005.

[23] S. Hadap, M.-P. Cani, M. Lin, T.-Y. Kim, F. Bertails, S. Marschner, K. Ward, and Z. Kačić-Alesić, "Strands and hair: modeling, animation, and rendering," in *ACM SIGGRAPH 2007 courses*, pp. 1–150, 2007.

[24] C. N.-T. G. S. Group *et al.*, "The effectiveness of intraocular pressure reduction in the treatment of normal-tension glaucoma," *American journal of ophthalmology*, vol. 126, no. 4, pp. 498–505, 1998.

[25] D. A. Lee and E. J. Higginbotham, "Glaucoma and its treatment: a review," *American journal of health-system pharmacy*, vol. 62, no. 7, pp. 691–699, 2005.

[26] T. Yamamoto and Y. Kitazawa, "Vascular pathogenesis of normal-tension glaucoma: a possible pathogenetic factor, other than intraocular pressure, of glaucomatous optic neuropathy," *Progress in retinal and eye research*, vol. 17, no. 1, pp. 127–143, 1998.

[27] D. Rempel, L. Dahlin, and G. LUNDBORG, "Pathophysiology of nerve compression syndromes: response of peripheral nerves to loading," *JBJS*, vol. 81, no. 11, pp. 1600–10, 1999.

[28] L. Dahlin and G. Lundborg, "The neurone and its response to peripheral, nerve compression," *The Journal of Hand Surgery: British & European Volume*, vol. 15, no. 1, pp. 5–10, 1990.

[29] G. Lundborg and L. B. Dahlin, "The pathophysiology of nerve compression," *Hand clinics*, vol. 8, no. 2, pp. 215–227, 1992.

[30] D. C. Liu and J. Nocedal, "On the limited memory bfgs method for large scale optimization," *Mathematical programming*, vol. 45, no. 1-3, pp. 503–528, 1989.

[31] J. M. Edgar and I. R. Griffiths, "Chapter 7 - white matter structure: A microscopist's view," in *Diffusion MRI (Second Edition)* (H. Johansen-Berg and T. E. Behrens, eds.), pp. 127–153, San Diego: Academic Press, second edition ed., 2014.